Characterization of N^+ Abundances in the Terrestrial Polar Wind using the Multiscale Atmosphere-Geospace Environment

R. M. Albarran[1], R. H. Varney[1], K. Pham[2], and D. Lin[2]

[1]University of California Los Angeles, Department of Atmospheric and Oceanic Sciences, Los Angeles, CA, United States
[2]National Center for Atmospheric Research, Boulder, CO, United States

Key Points:

- Simulated N^+ and O^+ densities increase while N^+ to O^+ density ratios decrease with solar activity.
- N^+ concentrations typically exceed He^+ densities and N^+ fluence rates versus solar activity qualitatively resemble those for O^+.
- The inclusion of metastable chemical production of N^+ is critical to numerically reproduce observations.

Corresponding author: Robert Albarran, albarran1@atmos.ucla.edu

Abstract

The High-latitude Ionosphere Dynamics for Research Applications (HIDRA) model is part of the Multiscale Atmosphere-Geospace Environment (MAGE) model under development by the Center for Geospace Storms (CGS) NASA DRIVE Science Center. This study employs HIDRA to simulate upflows of H^+, He^+, O^+, and N^+ ions, with a particular focus on the relative N^+ concentrations, production and loss mechanisms, and thermal upflow drivers as functions of season, solar activity, and magnetospheric convection. The simulation results demonstrate that N^+ densities typically exceed He^+ densities, N^+ densities are typically $\sim$ 10% O^+ densities, and N^+ concentrations at quiet-time are approximately 50-100% of N^+ concentrations during storm-time. Furthermore, the N^+ and O^+ upflow fluxes show similar trends with variations in magnetospheric driving. The inclusion of ion-neutral chemical reactions involving metastable atoms is shown to have significant effects on N^+ production rates. With this metastable chemistry included, the simulated ion density profiles compare favorably with satellite measurements from Atmosphere Explorer C (AE-C) and Orbiting Geophysical Observatory 6 (OGO-6).

1 Introduction & Motivation

The ionosphere represents a significant source of ions in the magnetosphere [Chappell et al., 1987]. Transport of ionospheric plasma to the magnetosphere is a multistep process characterized by the ionospheric heating, expansion, and upflow of ions, followed by ion energization to escape energies [Strangeway et al., 2005] [Zheng et al., 2005]. Type 1 ion upflow and ionospheric expansion is due to frictional heating from differential ion-neutral drifts [Wahlund et al., 1992] [Zettergren & Semeter, 2012]. Type 2 ion upflow is caused by field-aligned ambipolar electric fields generated from ionospheric electrons heated by soft particle precipitation [Su et al., 1999]. Ion upflow has primarily been observed in the cusp or midnight auroral zone with ion velocities of $\sim$ 100-750 $m \cdot s^{-1}$ below 1000 km [Ogawa et al., 2003] [Foster & Lester, 1996]. Ion outflow occurs above the upflow altitudes where additional forces are required to accelerate ions above escape velocity. These forces can be auroral acceleration region parallel electric fields forming $\sim$ 1-10 keV ion beams [McFadden et al., 1998], or a combination of perpendicular acceleration and the magnetic mirror force forming ion conic distributions from $\sim$ 10-1000 eV [Yau & Andre, 1997] [André & Yau, 1997]. Perpendicular acceleration can be provided by ion cyclotron resonance heating from broadband extremely low-frequency (BBELF) or very low-frequency (VLF) waves [Crew et al., 1990] [Kintner et al., 1996] [André et al., 1998], or by lower hybrid plasma waves [Lynch et al., 1996] [Lynch et al., 1999].

Ionospheric outflow at polar latitudes has been an avid subject of theoretical and experimental study since it was predicted [Dessler & Michel, 1966] [Nishida, 1966]. First evidence of ionospheric plasma populating the magnetosphere was inferred by [Shelley et al., 1972] through observations of precipitating keV O^+ fluxes exceeded H^+ flux values. This was confirmed by $>$ 0.5 keV upflowing H^+ and O^+ ions above 5000 km observed by the polar-orbiting S3-3 satellite [Yau & Andre, 1997] where observations demonstrated ion velocity distribution peaks along the upward magnetic field line direction (ion beams) [Shelley et al., 1976] and distribution peaks at angles to the magnetic field lines (ion conics) [Sharp et al., 1977].

The last five decades of ionospheric ion outflow study has demonstrated that outflow from the Earth's ionosphere to magnetosphere is highly variable in composition, energy, space, and time. Observations have shown that ion outflow is dependent on solar cycle, season, and geomagnetic activity [Yau et al., 1985] [Collin et al., 1998]. Although it is considered that the solar wind enters the magnetosphere to deposit a significant amount of energetic ions to the plasma sheet [Eastman et al., 1985] [Kivelson & Spence, 1988] [Lennartsson, 2001], the solar wind source alone is not sufficient to supply the plasma sheet and ring current with observed O^+ levels [Shelley et al., 1972]. Measurements taken in the 1980s from the DE-1 satellite suggest the plasma in the plasmasphere, plasma trough, plasma sheet, and magnetotail lobes may be sufficiently supplied by the ionosphere [Huddleston et al., 2005]. It is suggested that all regions of the magnetosphere may be supplied by ionospheric ions except for the inner radiation belt [Huddleston et al., 2005].

The enlarged cusp/cleft region in the dayside auroral zone between ∼ 9-15 hours magnetic local time (MLT) extending a few degrees in latitude [Bouhram et al., 2003] has been identified as a major source of ionospheric ions for the magnetosphere [Lockwood et al., 1985] [Thelin et al., 1990]. Magnetospheric energy may be deposited to the high-latitude ionosphere by precipitating charged particles, field-aligned currents, or Alfvén waves [Zheng et al., 2005]. The presence of heavy ionospheric ions has roles in magnetospheric dynamics [M. Y. Lin et al., 2020]: by affecting wave propagation [Bashir & Ilie, 2018] [Keika et al., 2011] [Summers et al., 2007] [Garcia et al., 2010], reconnection rates by mass loading [Garcia et al., 2010] [Nosé et al., 2005] [Winglee et al., 2002] [Wiltberger et al., 2010], ring current dynamics [Daglis et al., 1999] [Hamilton et al., 1988] [Kistler et al., 1989] [Liemohn et al., 1999], and cross polar cap potential (CPCP) [Glocer et al., 2009] [Ilie et al., 2013] [Winglee et al., 2002].

Heavy ionospheric ion outflows are typically N^+ or O^+, which have different behaviors because of their 12% mass difference [Ilie & Liemohn, 2016]. Most previous observations are limited to low mass resolution measurements, thus unable to properly distinguish N^+ from O^+ [M. Y. Lin et al., 2020] [Ilie & Liemohn, 2016] [Yamauchi, 2019]. During quiet times, the Orbiting Geophysical Observatory (OGO-2) and Explorer 31 observed significant N^+ between 500-1400 km above 60° latitude with N^+ densities around 5-30% of O^+ densities [Brinton et al., 1968] [Brinton et al., 1971] [Hoffman, 1967]. Ion mass spectrometer data on the NASA International Satellite for Ionospheric Studies (ISIS-2) indicate N^+ abundances consistently ∼10% of O^+ densities for all variations of environments [Hoffman, 1970] [Hoffman et al., 1974]. N^+ has been reported to dramatically increase during storm time [Hoffman et al., 1974]. In this study, we employ High-latitude Ionosphere Dynamics for Research Applications (HIDRA) (formerly, IPWM [Varney et al., 2014] [Varney et al., 2015] [Varney et al., 2016]) to simulate N^+ upflows.

2 Model Description and Simulation Setup

The High-latitude Ionosphere Dynamics for Research Applications (HIDRA) model is a significant rewrite of the ionosphere/polar wind model (IPWM) [Varney et al., 2014] [Varney et al., 2015] [Varney et al., 2016]) and designed as a component of the Multiscale Atmosphere-Geospace Environment (MAGE) framework under development by the Center for Geospace Storms NASA DRIVE Science Center. HIDRA models the parallel and perpendicular transport of plasma in a 3-D Eulerian grid using finite volume methods. The parallel transport scheme in HIDRA is identical to IPWM [Varney et al., 2014] and solves eight-moment fluid equations for the number densities, parallel velocity, temperatures, and parallel heat fluxes of ions and electrons. The photochemistry in HIDRA is identical to IPWM with one correction. HIDRA uses the High Resolution Extreme Ultraviolet Model for Aeronomic Calculations (HEUVAC) solar spectrum [Richards et al., 2006], the chemical reactions for $O^+(^4S)$, $O^+(^2D)$, $O^+(^2P)$, N^+, N_2^+, O_2^+, and NO^+ following [Richards, 2011], and additional chemical reactions for H^+ and He^+ as explained by [Varney et al., 2014]. Unfortunately IPWM accidentally used a charge exchange rate for $N^+ + O \rightarrow N + O^+$ that was 2 orders of magnitude too high, resulting in erroneously low levels of N^+. HIDRA corrects this mistake and uses the reaction rate recommended by [Richards, 2011]. HIDRA solves for the full transport of H^+, He^+, $O^+(^4S)$, and N^+, and assumes chemistry is faster than transport for the other ions. By contrast, IPWM included the chemistry of N^+ but ignored its transport. The HIDRA runs presented here ignore wave particle interactions and other non-classical ion acceleration mechanisms.

HIDRA employs the same non-orthogonal magnetic coordinate system as IPWM [Varney et al., 2015], but the perpendicular grid construction and perpendicular transport numerical methods have been thoroughly rewritten using the partial interface method, similar to the Grid Agnostic Magnetohydrodynamics for Extended Research Applications (GAMERA) model [Zhang et al., 2019]. Unlike the cell-centered approach in IPWM, the rewritten scheme tracks different quantities on cell corners, cell edges, and cell centers. Electrostatic potential is specified on the cell corners. The electric fields parallel to the cell edges are computed from the potential differences between the corners. These edge-parallel electric fields determine the component of the $\mathbf{E} \times \mathbf{B}$ drift normal to the cell face since the cell faces are parallel to the dipole magnetic field

by construction. The flux of a conserved quantity Q (e.g. number density) through a cell face is computed as the face area times the normal component of the $\mathbf{E} \times \mathbf{B}$ drift times the conserved quantity reconstructed at the cell edge. The quantities at the cell edges are reconstructed from the cell-centered quantities using the same techniques as GAMERA. The grid singularity at the pole is treated by having the cells adjacent to the pole as triangles instead of quadrilaterals, and the potential at the pole is identical for every cell with a triangle tip at the pole. This treatment has proven to be robust, unlike the original IPWM treatment which could produce numerical artifacts near the pole when run at high resolution. Lastly, IPWM fixed the equatorward boundary of the grid at $L = 4$, whereas HIDRA allows the equatorward boundary to be adjustable. The simulations presented here use an equatorward boundary at $L = 3$ (54.7° invariant latitude). The equatorward boundary at is a hard wall, meaning that transport of plasma from the mid-latitudes to the high-latitudes is neglected. For the moderately active storms simulated in this paper the high-latitude convection does not expand to $L = 3$, but this model configuration would not be appropriate for larger storms. HIDRA is operated at 'quad' spatial resolution: 82 altitude bins with resolution of $\sim$ 18 km at the lower boundary of $\sim$ 97 km and $\sim$ 743 km at the upper boundary of $\sim$ 8400 km, 32 latitude bins with resolution of $\sim$ 1.09° in the northern geographic hemisphere, and 128 longitude bins with resolution of $\sim$ 2.8°. The lower boundary is set by chemical equilibrium, and the upper boundary is open.

HIDRA requires inputs from a variety of models. GAMERA [Zhang et al., 2019] is a global magnetospheric magnetohydrodynamics model driven by upstream solar wind inputs. The inner boundary conditions for GAMERA are determined by the REMIX model, which is a redeveloped version of the Magnetosphere Ionosphere Exchange (MIX) model [Merkin & Lyon, 2010]. REMIX solves a 2-D electrostatic potential given field-aligned currents (FAC) computed from $\nabla \times \mathbf{B}$ at the inner boundary of GAMERA and conductances computed from the precipitation model. For the simulations presented here, the neutral densities and temperatures are provided by NRLMSISE-00 [Picone et al., 2002], and the neutral winds are set to zero. Both HEUVAC and NRLMSISE-00 are parameterized by the daily $F_{10.7}$ and 81-day averaged $F_{10.7A}$ indexes, which are equal for the runs in this work. NRLMSISE-00 also requires the planetary A_p index. All of the runs here use $A_p = 4.0$ representing quiet thermospheric conditions. The simulations presented here use potentials and precipitation inputs from an existing GAMERA-REMIX (GR) configuration of the MAGE model run. The GR configuration of the MAGE model couples GAMERA, the Rice Convection Model (RCM) [Toffoletto et al., 2003] of the inner magnetosphere, and REMIX. However, the GR configuration does not include the Thermosphere-Ionosphere Electrodynamics General Circulation (TIEGCM) model. This does not affect our results as the HIDRA model currently uses NRLMSISE-00 to provide the necessary neutral densities and temperature. HIDRA takes potential and precipitation inputs from REMIX outputs, and uses empirical relations to compute production rates by impact ionization of precipitating electrons [Fang et al., 2008]. The electron precipitation used in this outflow study includes both mono-energetic and diffuse electron precipitation [D. Lin et al., 2021]. The mono-energetic electron precipitation is derived from the MHD FAC and thermal population by solving for the Fridman-Lemaire relation in a similar manner to [Zhang et al., 2015]. The diffuse electron precipitation is derived with the RCM model by taking into account energy-dependent convection drift of electrons in the inner magnetosphere [Bao, 2019]. The mono-energetic and diffuse electron precipitation are then merged to give a global auroral distribution. More details of the precipitation model can be found in [D. Lin et al., 2021]. This is the precipitation configuration used for [Pham et al., 2022] and [D. Lin et al., 2022]. Further details of GAMERA-REMIX coupling are given by [Merkin & Lyon, 2010] and details of the MAGE model can be found in [Pham et al., 2022].

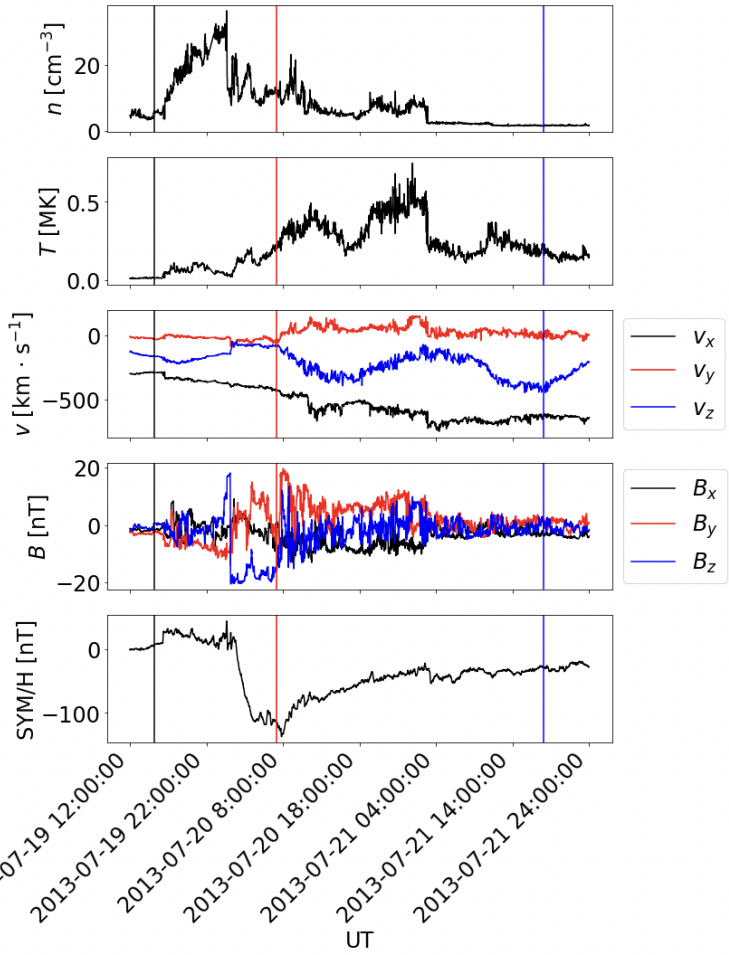

Figure 1: Solar wind parameters used to drive GAMERA-REMIX, presented in solar magnetic (SM) coordinates. Panels show a) proton density, b) proton temperature, c) solar wind velocity, and d) interplanetary magnetic field. Also shown for context is the Sym/H index (e), but this is not an input to GAMERA. The horizontal axis shows the shifted time for summertime HIDRA simulations (i.e. beginning at 19 July 2013 12:00:00 UT). Vertical lines indicate three times on interest for future comparison: quiet time (t_1 = 2013-07-19 14:00:00 UT), storm time (t_2 = 2013-07-20 06:00:00 UT), and recovery-time (t_3 = 2013-07-21 17:00:00 UT). For the wintertime runs these times become t_1 = 2013-12-19 14:00:00 UT, t_2 = 2013-12-20 06:00:00 UT, and t_3 = 2013-12-21 17:00:00 UT.

Each of the HIDRA runs in this paper use identical GAMERA-REMIX outputs from a single simulation driven by the solar wind driving conditions shown in Figure 1. We have extracted the 72 hours starting at 31 May 2013 12:00:00 UT from this longer 27-day run, and we have shifted the REMIX outputs in time to nominally begin at either 19 July 2013 12:00:00 UT for summertime runs or 19 December 2013 12:00:00 UT for wintertime runs. Performing July and December runs permits a direct comparison with [M. Y. Lin et al., 2020]. The June 2013 event serves as a proxy for N^+ upflow fluxes during different solar wind driving conditions; in UT, we are calling summer (winter) quiet-time at t_1 = 2013-07-19 (2013-12-19) 14:00:00 UT, storm-time at t_2 = 2013-07-20 (2013-12-20) 06:00:00 UT, and recovery-time at t_3 = 2013-07-21 (2013-12-21) 17:00:00 UT. For summer and winter we perform runs using $F_{10.7}$ = 80 sfu, $F_{10.7}$ = 120 sfu, and $F_{10.7}$ = 200 sfu, where the solar flux unit (sfu) is 10^{-22} W · m^{-2} · Hz^{-1}.

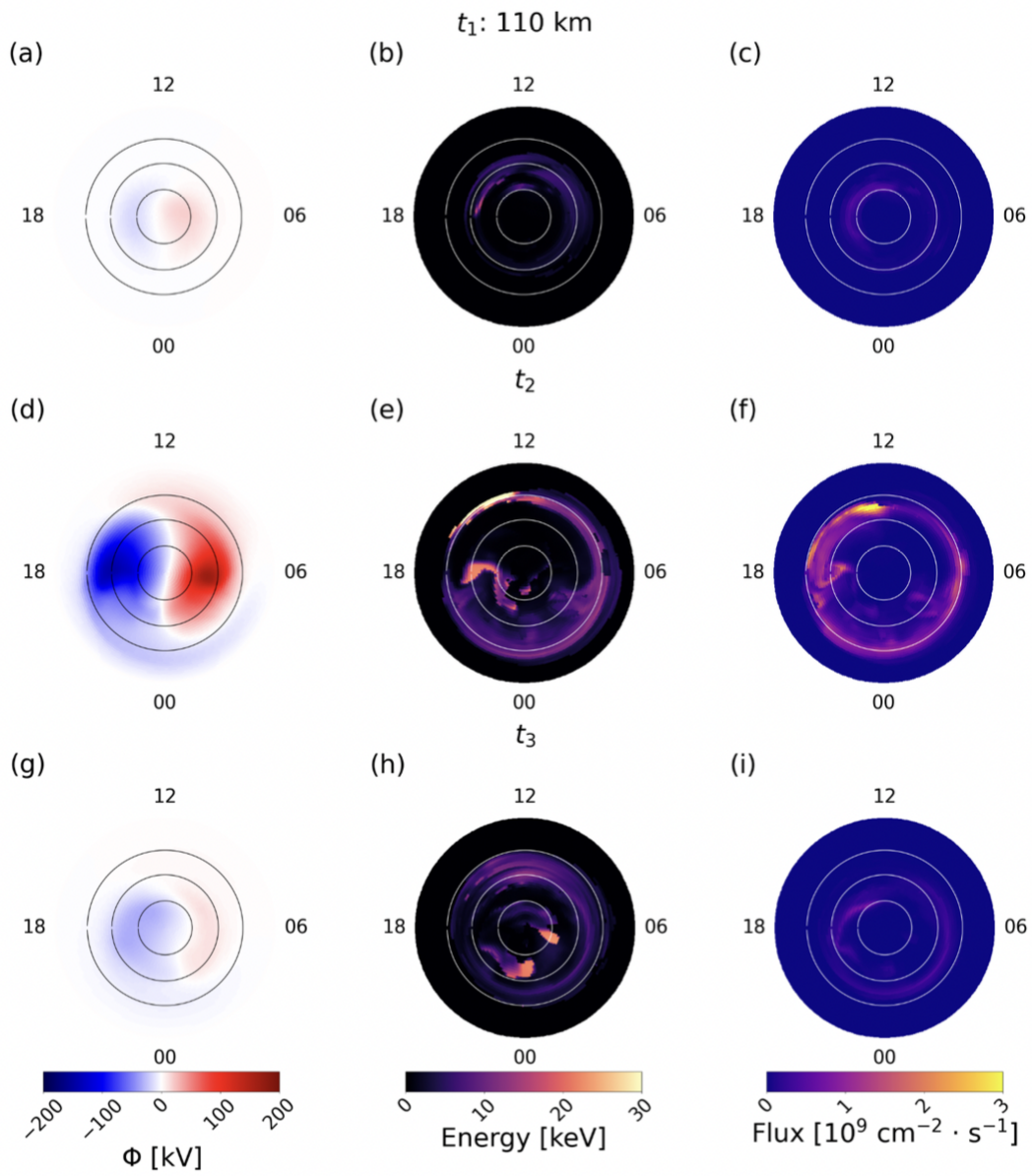

Figure 2: REMIX potential, Φ, in Panels (a), (d), and (g), average precipitation energy in Panels (b), (e), and (h), and precipitation number flux in Panels (c), (f), and (i) at the REMIX altitude of 110 km during quiet-time (at time t_1) in Panels (a), (b), and (c), storm-time (at time t_2) in Panels (d), (e), and (f), and recovery-time (at time t_3) in Panels (g), (h), and (i).

HIDRA is 'spun-up' for ∼ 12 hours from non-equilibrium initial conditions and reaches steady-state before introducing convection from REMIX. The REMIX potential, average precipitation energy and number flux, used to drive HIDRA is shown in Figure 2. For Figure 2 and those that follow, circles are shown for 60°, 70°, and 80° magnetic latitudes in the northern hemisphere. The value of $F_{10.7}$ selected corresponds to that used to call the neutral thermosphere parameters from NRLMSISE-00 and the solar zenith angle. Both seasons take identical magnetospheric boundary conditions at times of interest in the geomagnetic storm.

3 Results

We analyze the results of the six simulations by focusing on snapshots at three representative times, quiet time (t_1), storm time (t_2), and recovery (t_3), indicated by the vertical lines in Figure 1. These three representative times bracket the observed behaviors over the full runs.

3.1 Relative Abundances of N^+ to O^+

To capture N^+ upflow characteristics during different geomagnetic conditions, we compare altitude slices of O^+ and N^+ densities at 1200 km for $F_{10.7} = 80$ sfu, $F_{10.7} = 120$ sfu, and $F_{10.7} = 200$ sfu and $A_p = 4$. Figures 3, 5, and 7 illustrate summertime N^+ to O^+ density ratios for $F_{10.7} = 80$ sfu in Panels (c), $F_{10.7} = 120$ sfu in Panels (f), and $F_{10.7} = 200$ sfu in Panels (i) for times t_1, t_2, and t_3, respectively. Similarly, Figures 4, 6, and 8 shows wintertime N^+ to O^+ density ratios for $F_{10.7} = 80$ sfu in Panels (c), $F_{10.7} = 120$ sfu in Panels (f), and $F_{10.7} = 200$ sfu in Panels (i) for times t_1, t_2, and t_3, respectively.

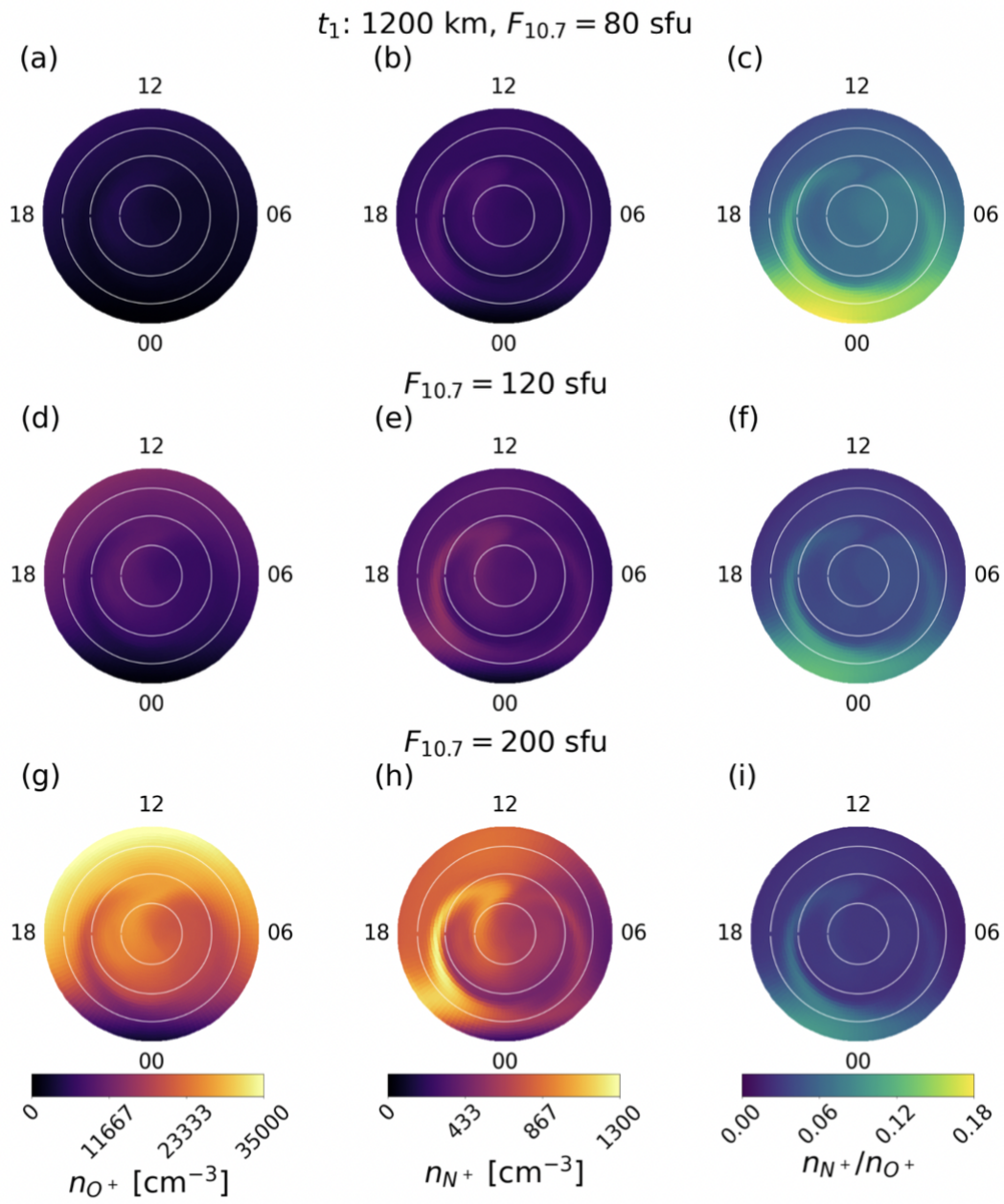

Figure 3: O^+ densities, n_{O^+}, in Panels (a), (d), and (g), N^+ densities, n_{N^+}, in Panels (b), (e), and (h), and O^+ to N^+ density ratios, n_{N^+}/n_{O^+}, in Panels (c), (f), and (i) at 1200 km during summer quiet-time geomagnetic conditions (at time t_1) for $F_{10.7}$ = 80 sfu in Panels (a), (b), and (c), $F_{10.7} = 120$ sfu in Panels (d), (e), and (f), and $F_{10.7} = 200$ sfu in Panels (g), (h), and (i).

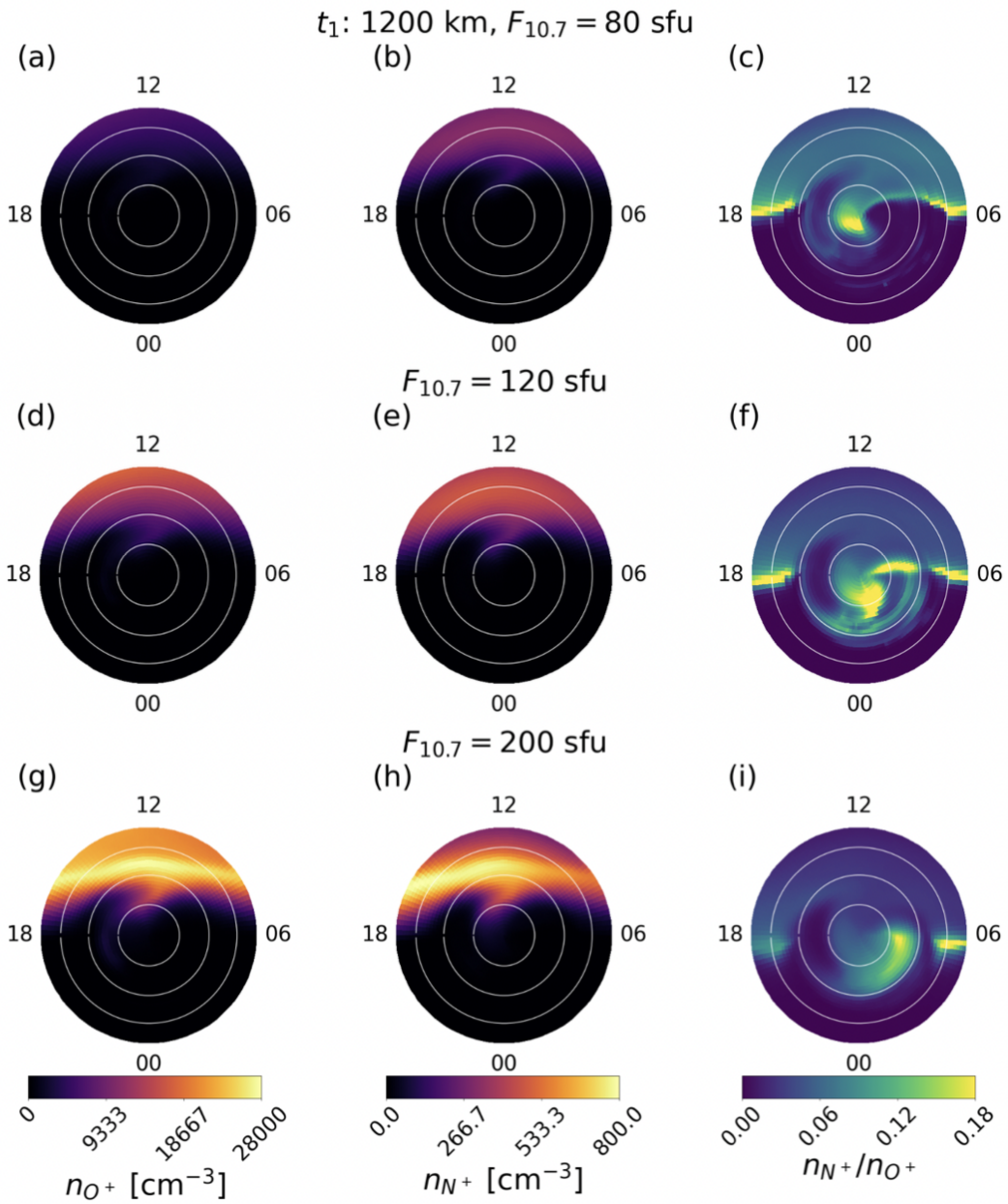

Figure 4: O^+ densities, n_{O^+}, in Panels (a), (d), and (g), N^+ densities, n_{N^+}, in Panels (b), (e), and (h), and O^+ to N^+ density ratios, n_{N^+}/n_{O^+}, in Panels (c), (f), and (i) at 1200 km during winter quiet-time geomagnetic conditions (at time t_1) for $F_{10.7}$ = 80 sfu in Panels (a), (b), and (c), $F_{10.7}$ = 120 sfu in Panels (d), (e), and (f), and $F_{10.7}$ = 200 sfu in Panels (g), (h), and (i).

Figure 3 shows that quiet-time (t_1) N^+ densities are ~ 10-14% of O^+ densities for $F_{10.7}$ = 80 sfu and n_{N^+}/n_{O^+} values decrease to less than 10% for $F_{10.7}$ = 120 sfu and $F_{10.7}$ = 200 sfu. As seen in Figure 4, quiet-time (t_1) N^+ densities are ~ 10-14% of O^+ densities for $F_{10.7}$ = 80 sfu. n_{N^+}/n_{O^+} values decrease, primarily in the pre and post-noon sectors, for $F_{10.7}$ = 120 sfu and $F_{10.7}$ = 200 sfu. In the absence of plasma production by photoionization near the midnight (0 hours MLT) sector, O^+ densities are low. Thus, the density ratios in Panels (c), (f), and (i) should be accepted with caution near local midnight.

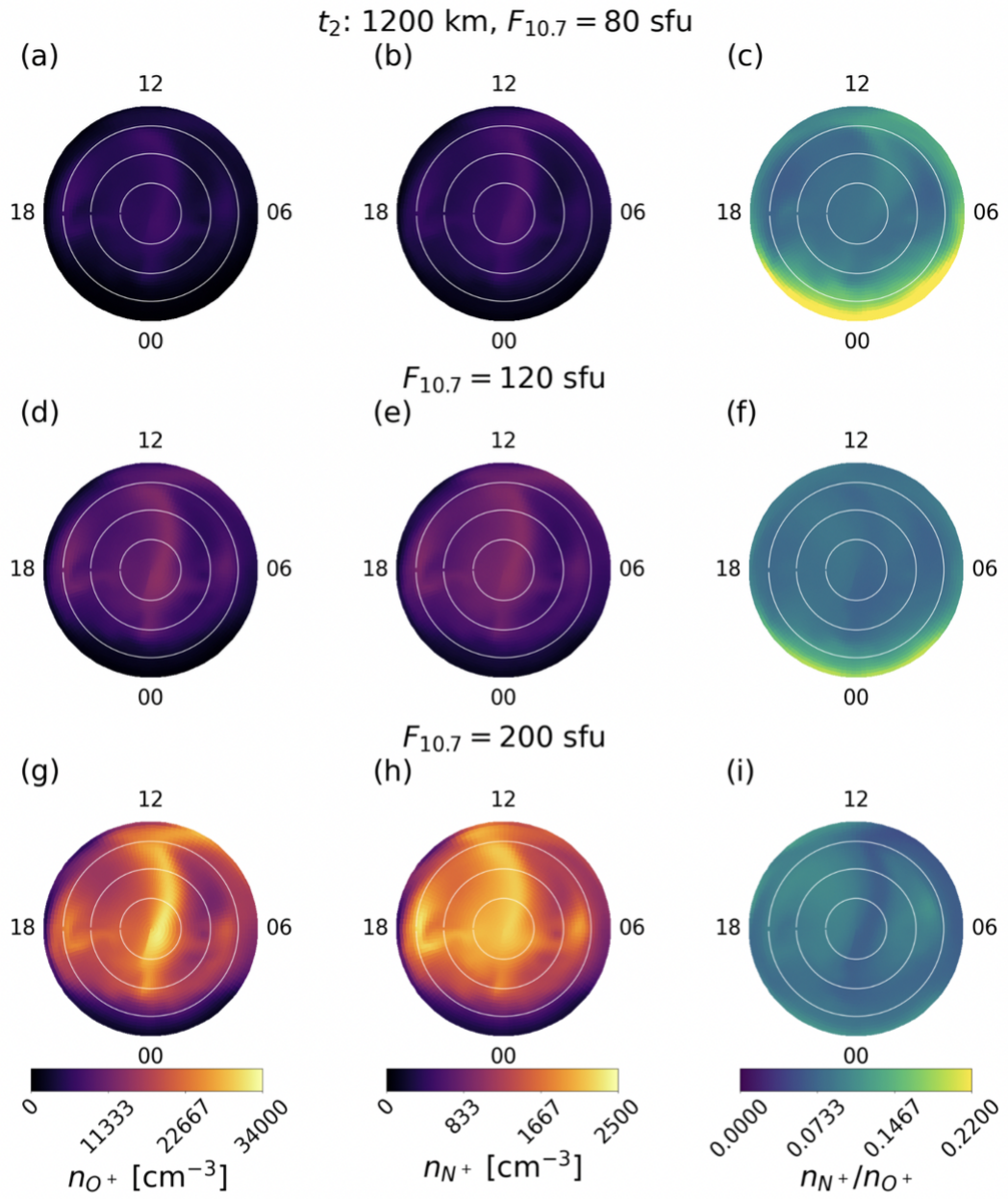

Figure 5: O^+ densities, n_{O^+}, in Panels (a), (d), and (g), N^+ densities, n_{N^+}, in Panels (b), (e), and (h), and O^+ to N^+ density ratios, n_{N^+}/n_{O^+}, in Panels (c), (f), and (i) at 1200 km during summer storm-time geomagnetic conditions (at time t_2) for $F_{10.7}$ = 80 sfu in Panels (a), (b), and (c), $F_{10.7} = 120$ sfu in Panels (d), (e), and (f), and $F_{10.7} = 200$ sfu in Panels (g), (h), and (i).

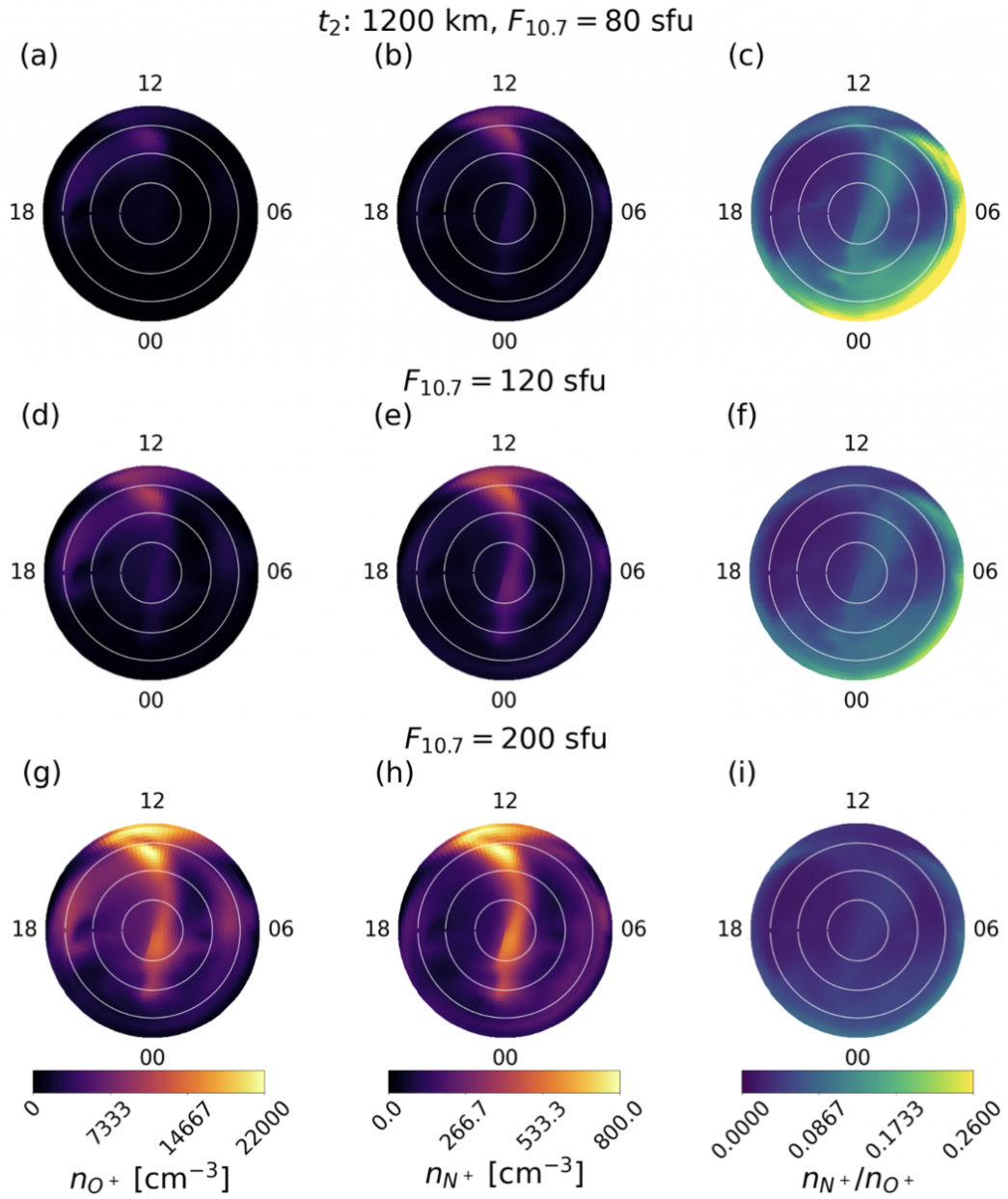

Figure 6: O^+ densities, n_{O^+}, in Panels (a), (d), and (g), N^+ densities, n_{N^+}, in Panels (b), (e), and (h), and O^+ to N^+ density ratios, n_{N^+}/n_{O^+}, in Panels (c), (f), and (i) at 1200 km during winter storm-time geomagnetic conditions (at time t_2) for $F_{10.7}$ = 80 sfu in Panels (a), (b), and (c), $F_{10.7} = 120$ sfu in Panels (d), (e), and (f), and $F_{10.7} = 200$ sfu in Panels (g), (h), and (i).

During summer storm-time (t_2), N^+ densities are $\sim$ 8-16% of O^+ densities for $F_{10.7}$ = 80 sfu, as seen in Panel (c) of Figure 5. N^+ densities are $\sim$ 7-12% of O^+ densities for $F_{10.7}$ = 120 sfu and $F_{10.7} = 200$ sfu, as seen in Panels (f) and (i) in Figure 5. During winter storm-time (t_2), N^+ densities are $\sim$ 8-14% of O^+ densities for $F_{10.7} = 80$ sfu, as seen in Panel (c) of Figure 6. N^+ densities are $\sim$ 6-12% of O^+ densities for $F_{10.7} = 120$ sfu and decrease to below 10% for $F_{10.7}$ = 200 sfu, as seen in Panels (f) and (i), respectively, in Figure 6. As the convection potential increases significantly in storm-time, the storm convection pattern moves equator-ward. In the process, cold mid-latitude plasma is transported pole-ward to create a tongue of ioniza-

tion (TOI). TOIs of N^+ and O^+ are visible along the noon-midnight direction with enhanced densities during storm-time, particularly for winter and $F_{10.7} = 200$ sfu, as seen in Panels (g) and (h) of Figure 6. TOIs are known to extend pole-ward across the polar cap from the day-side storm-enhanced density (SED) anomaly. Fragmentations of the TOI contributes to the formation of polar plasma patches that may produce scintillation, which can negatively affect satellite communications and navigation signals at high latitudes [Pokhotelov et al., 2021].

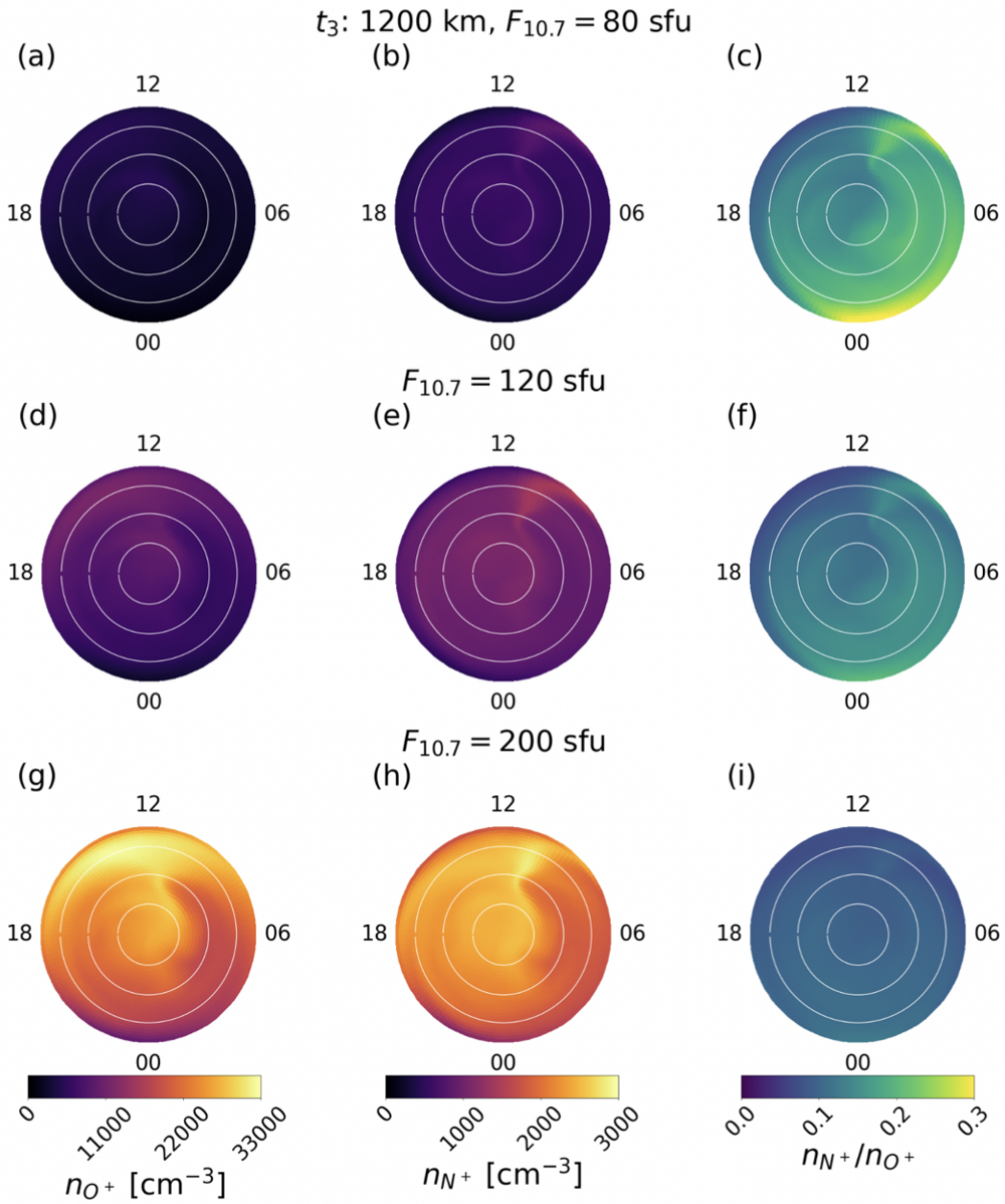

Figure 7: O^+ densities, n_{O^+}, in Panels (a), (d), and (g), N^+ densities, n_{N^+}, in Panels (b), (e), and (h), and O^+ to N^+ density ratios, n_{N^+}/n_{O^+}, in Panels (c), (f), and (i) at 1200 km during summer recovery-time geomagnetic conditions (at time t_3) for $F_{10.7} = 80$ sfu in Panels (a), (b), and (c), $F_{10.7} = 120$ sfu in Panels (d), (e), and (f), and $F_{10.7} = 200$ sfu in Panels (g), (h), and (i).

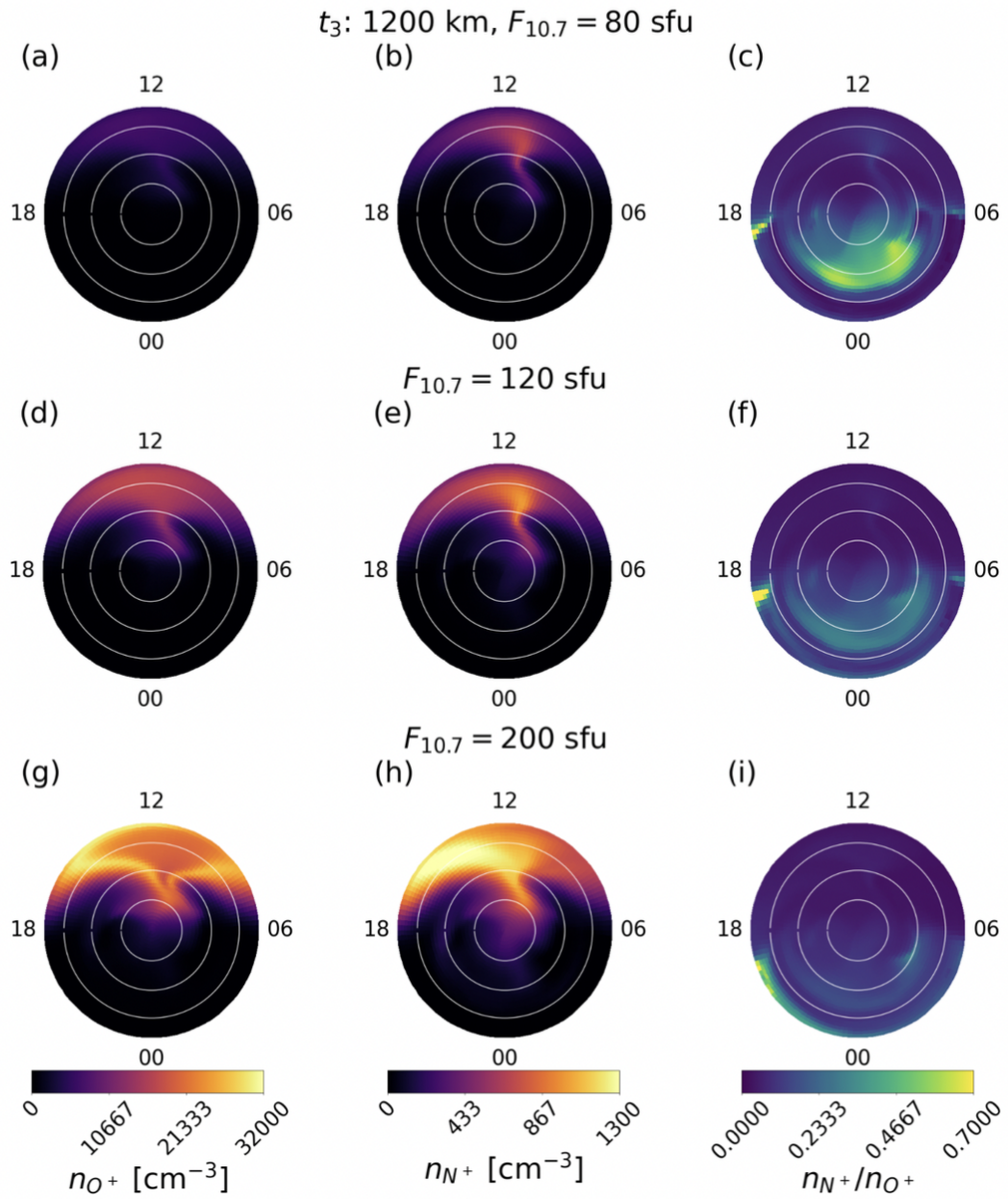

Figure 8: O^+ densities, n_{O^+}, in Panels (a), (d), and (g), N^+ densities, n_{N^+}, in Panels (b), (e), and (h), and O^+ to N^+ density ratios, n_{N^+}/n_{O^+}, in Panels (c), (f), and (i) at 1200 km during winter recovery-time geomagnetic conditions (at time t_3) for $F_{10.7} = 80$ sfu in Panels (a), (b), and (c), $F_{10.7} = 120$ sfu in Panels (d), (e), and (f), and $F_{10.7} = 200$ sfu in Panels (g), (h), and (i).

During summer recovery-time (t_3), relative N^+ to O^+ concentrations are greatest for $F_{10.7} = 80$ sfu where n_{N^+}/n_{O^+} values are $\sim$ 15-30%, as seen in Panel (c) of Figure 7. N^+ densities are less than $\sim$ 20% of O^+ concentrations for $F_{10.7} = 120$ sfu, as seen in Panel (f), and less than $\sim$ 15% for $F_{10.7} = 200$ sfu, as seen in Panel (i). During winter recovery-time (t_3), N^+ densities are $\sim$ 5% of O^+ densities for all values of $F_{10.7}$. In general, the relative abundances of N^+ to O^+ are in agreement with numerical studies by [M. Y. Lin et al., 2020] and early measurements by OGO-2 [Brinton et al., 1968], Explorer 31 [Hoffman, 1967] [Hoffman, 1970], and ISIS-2 [Hoff-

man et al., 1974]. Panels (c), (f), and (i) of Figures 3, 5, 7, 4, 6, and 8 demonstrate that, although O^+ and N^+ densities increase with solar activity for both summer and winter, relative abundances of N^+ to O^+ are greater for lower $F_{10.7}$ values over all geomagnetic conditions and seasons. During increased solar activity, strong vertical temperature gradients must be balanced by strong density gradients to maintain a constant pressure profile. Since changes in the vertical density gradients of heavy species change more than the average density changes than for light species, vertical winds more significantly affect O/N_2 gradients at solar maximum than at solar minimum [Burns et al., 2015]. As a result, there are enhanced O/N_2 density ratios, and subsequently, decreased N^+/O^+ density ratios for higher $F_{10.7}$.

3.2 N^+ Densities During Storm-time

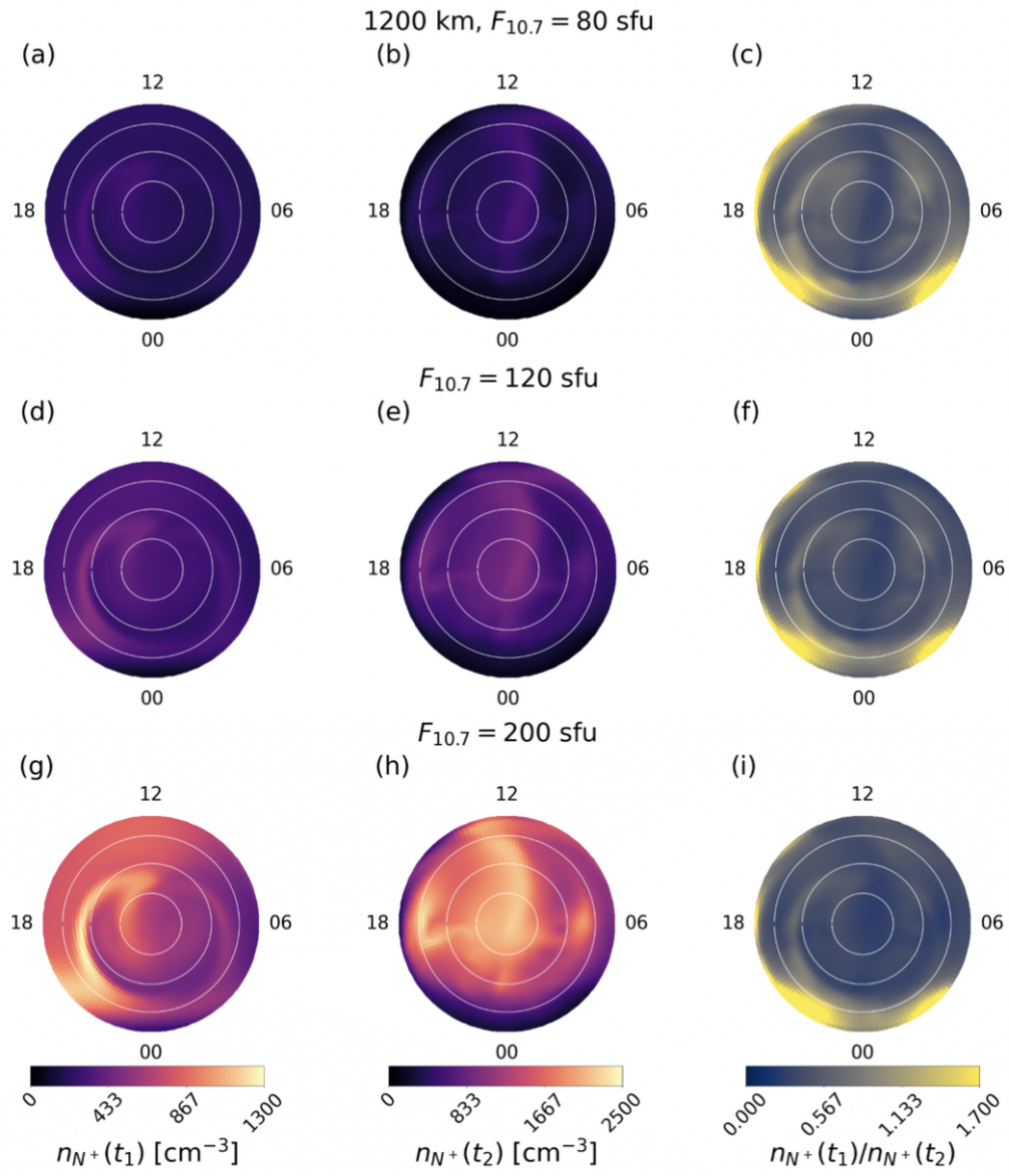

Figure 9: Summer N^+ densities at quiet-time, $n_{N^+}(t_1)$, in Panels (a), (d), and (g), N^+ densities at storm-time, $n_{N^+}(t_2)$, in Panels (b), (e), and (h), and quiet-time to storm-time N^+ density ratios, $n_{N^+}(t_1)/n_{N^+}(t_2)$, at 1200 km, in Panels (c), (f), and (i), for $F_{10.7}$ = 80 sfu in Panels (a), (b), and (c), $F_{10.7}$ = 120 sfu in Panels (d), (e), and (f), and $F_{10.7}$ = 200 sfu in Panels (g), (h), and (i).

Relative densities of N^+ during quiet-time (t_1) to storm-time (t_2) for $F_{10.7}$ = 80 sfu, $F_{10.7}$ = 120 sfu, and $F_{10.7}$ = 200 sfu at 1200 km during summer are shown in Figure 9. It is apparent that quiet-time N^+ densities are $\sim$ 50-100% of storm-time N^+ densities for all values of $F_{10.7}$ during summer, as seen in Panels (c), (f), and (i) in Figure 9. Relative densities of N^+ during quiet-time (t_1) to storm-time (t_2) for $F_{10.7}$ = 80 sfu, $F_{10.7}$ = 120 sfu, and $F_{10.7}$ = 200 sfu at 1200 km during winter are shown in Figure 10. Winter quiet-time N^+ densities exceed storm-time con-

centrations by up to $\sim$ 300% in the pre and post-noon sectors. However, night-side of the terminator, storm-time N^+ densities exceed quiet-time values by up to $\sim$ 80%, as seen in Panels (c), (f), and (i) of Figure 10. As seen in Figures 9 and 10, $n_{N^+}(t_1)/n_{N^+}(t_2)$ values remain largely unaltered with solar activity during summer and winter. The large increases of storm-time N^+ concentrations are consistent with early results by [Hoffman, 1970] and [Hoffman et al., 1974].

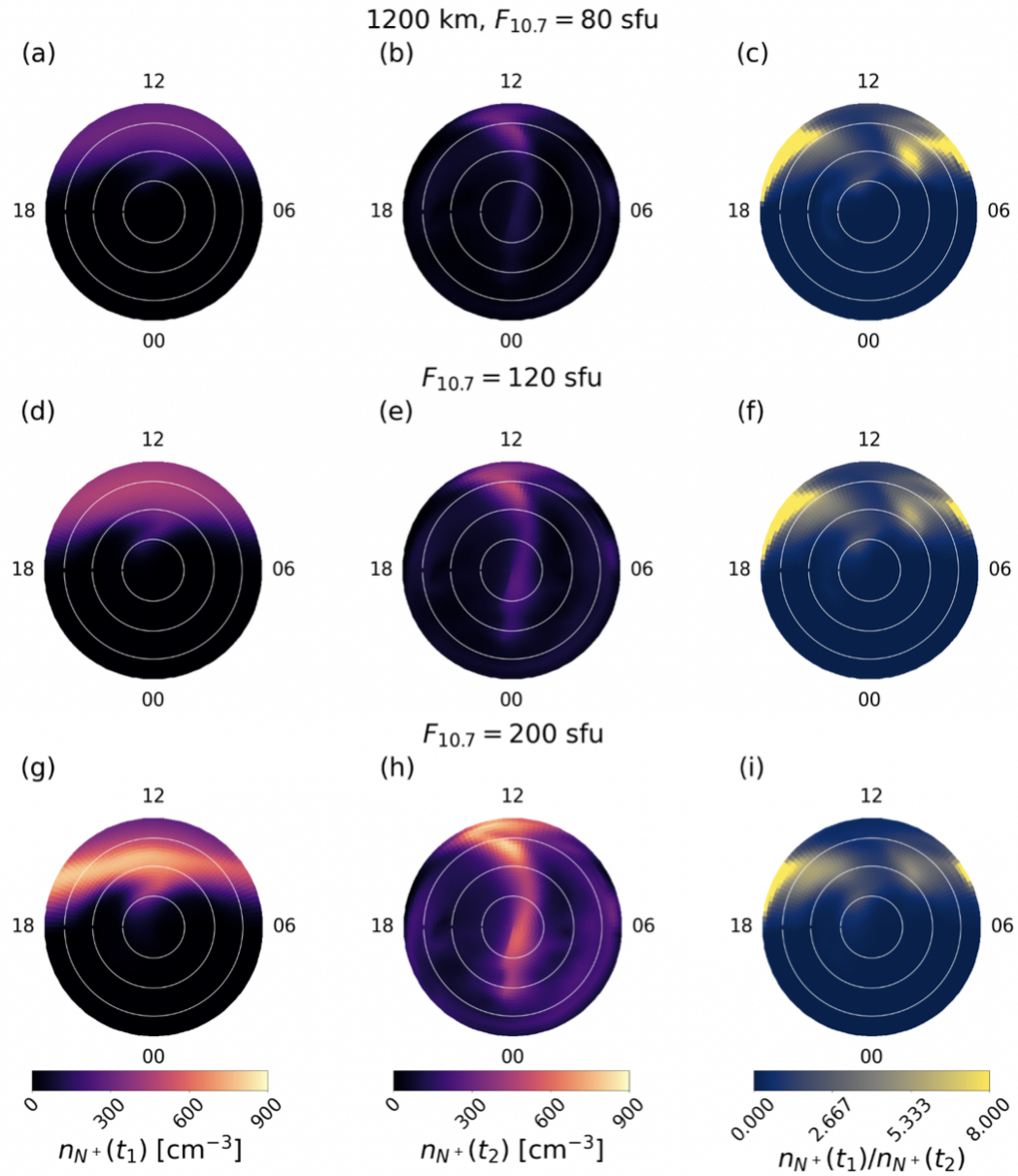

Figure 10: Winter N^+ densities at quiet-time, $n_{N^+}(t_1)$, in Panels (a), (d), and (g), N^+ densities at storm-time, $n_{N^+}(t_2)$, in Panels (b), (e), and (h), and quiet-time to storm-time N^+ density ratios, $n_{N^+}(t_1)/n_{N^+}(t_2)$, at 1200 km, in Panels (c), (f), and (i), for $F_{10.7}$ = 80 sfu in Panels (a), (b), and (c), $F_{10.7} = 120$ sfu in Panels (d), (e), and (f), and $F_{10.7} = 200$ sfu in Panels (g), (h), and (i).

3.3 Multi-Fluid Fluences & Fluxes

Figures 11 and 12 illustrate ion fluence rates for H^+, He^+, O^+, and N^+ ions at 1200 km for quiet-time (t_1), storm-time (t_2), and recovery-time (t_3) and $F_{10.7} = 80$ sfu, $F_{10.7} = 120$ sfu, and $F_{10.7} = 200$ sfu for northern hemisphere summer and winter, respectively. It is apparent from Panels (a) and (c) that H^+ fluence rates decrease with increasing $F_{10.7}$ due to enhanced temperatures with higher $F_{10.7}$. According to conservation of neutral H flux in the thermosphere, as the neutral H temperature increases with solar activity the neutral H density must decrease; neutral H densities decrease with $F_{10.7}$ due to the Jean's escape of neutral H with increased temperature [Nossal et al., 2012]. As a result, the charge exchange reaction $O^+ + H \rightarrow H^+ + O$ slows down which limits the production of H^+ with increasing $F_{10.7}$. Alternatively, heavy ions such as He^+, O^+, and N^+, have fluence rates that increase with $F_{10.7}$ since increased temperatures with greater solar activity results in greater scale heights. The trends of H^+, He^+, and O^+ fluences with $F_{10.7}$ are in qualitative agreement with results from [Yau et al., 1988].

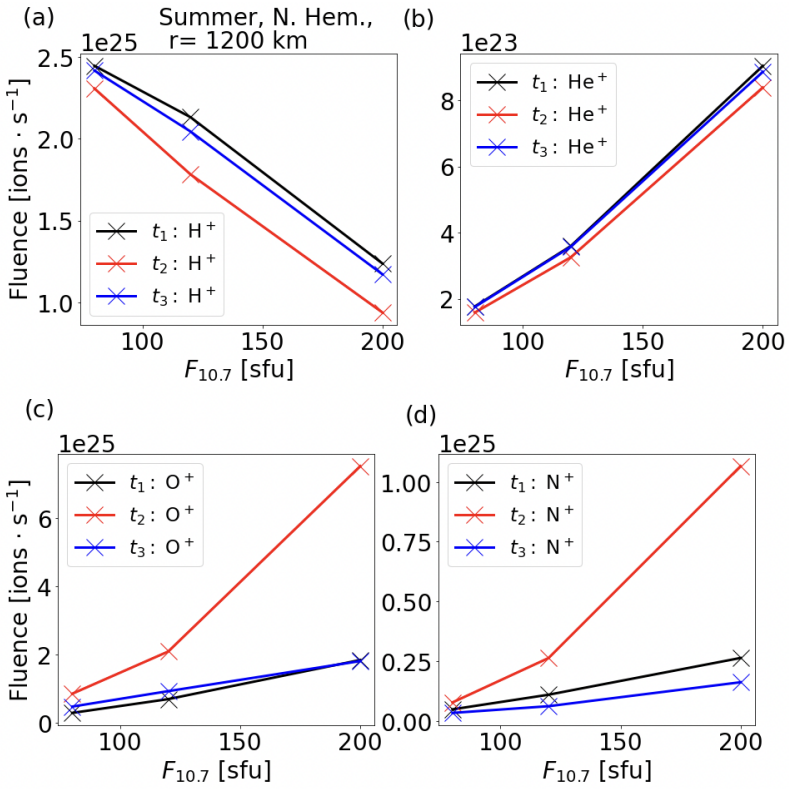

Figure 11: Summer ion fluence rates for quiet-time (t_1), storm-time (t_2), and recovery-time (t_3) at 1200 km altitude for H^+ in Panel (a), He^+ in Panel (b), O^+ in Panel (c), and N^+ in Panel (d) as functions of $F_{10.7}$ for $A_p = 4$ ($K_p = 1o$).

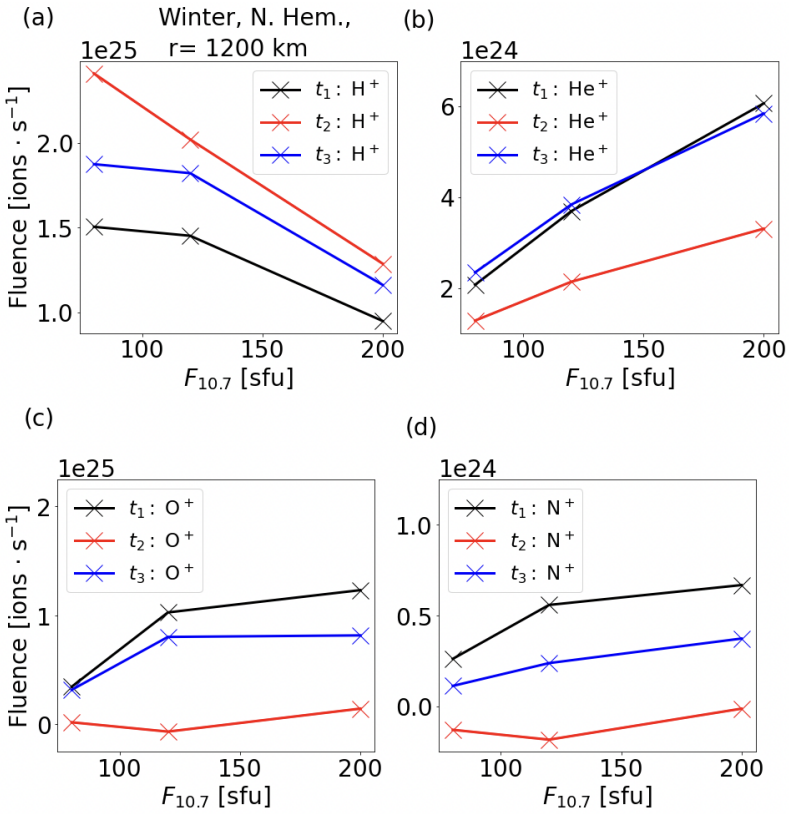

Figure 12: Winter ion fluence rates for quiet-time (t_1), storm-time (t_2), and recovery-time (t_3) at 1200 km altitude for H^+ in Panel (a), He^+ in Panel (b), O^+ in Panel (c), and N^+ in Panel (d) as functions of $F_{10.7}$ for $A_p = 4$ ($K_p = 1o$).

Although Figures 11 and 12 are for ions much cooler than 10 eV, they qualitatively agree with results from [Yau et al., 1988]. A static, quiet thermosphere specified by $A_p = 4$ is used such that neutral responses to storm-time are not captured. Nevertheless, the inclusion of thermospheric dynamics, particularly storm-time neutral density perturbations, is central to space weather modeling and predictions [Pham et al., 2022] [D. Lin et al., 2022]. N^+ fluences, like O^+, are strongly dependent on $F_{10.7}$, particularly during the enhanced convection at time t_2, as seen in Panels (c) and (d) of Figure 11. N^+ fluences are qualitatively similar to O^+ with varying solar activity at roughly an order of magnitude less. Neutral He concentrations in the winter hemisphere increase by 1 to 2 orders-of-magnitude relative to the summer hemisphere in a phenomena known as the helium winter bulge [Liu et al., 2014]. Increases in neutral He densities produce greater He^+ densities by photoionization. The winter helium bulge is expected to result in greater responses of He^+ with geomagnetic activity, as seen in the near-equal He^+ fluences during all summer geomagnetic conditions, seen in Panel (b) of Figure 11, and the decreased He^+ fluences during winter storm-time, as seen in Panel (b) of Figure 12.

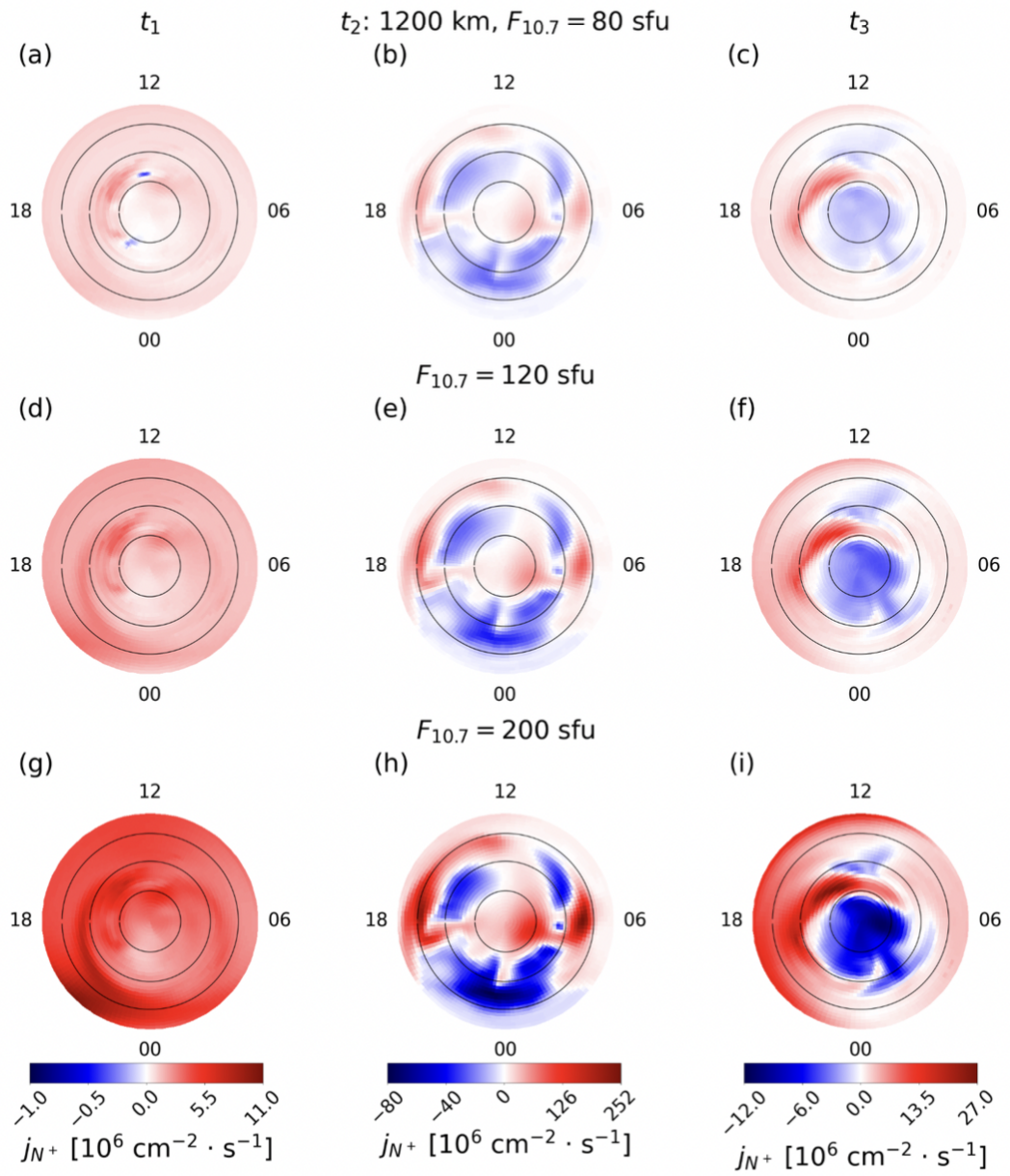

Figure 13: Summer N^+ fluxes, j_{N^+}, at 1200 km for $F_{10.7}$ = 80 sfu in Panels (a), (b), and (c), $F_{10.7}$ = 120 sfu in Panels (d), (e), and (f), and $F_{10.7}$ = 200 sfu in Panels (g), (h), and (i) during quiet-time (t_1) in Panels (a), (d), and (g), storm-time (t_2) in Panels (b), (e), and (h), and recovery-time (t_3) in Panels (c), (f), and (i).

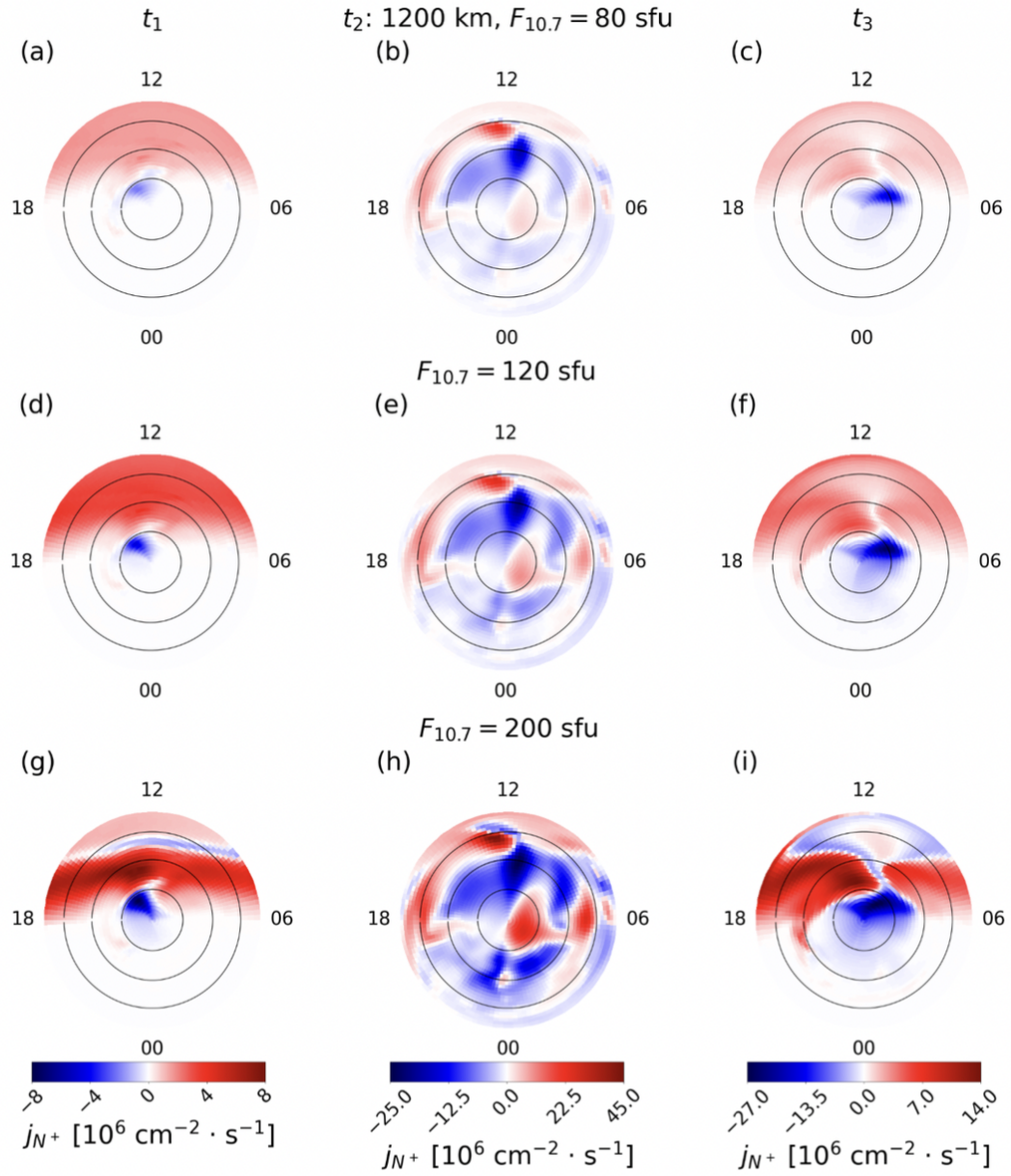

Figure 14: Winter N^+ fluxes, j_{N^+}, at 1200 km for $F_{10.7}$ = 80 sfu in Panels (a), (b), and (c), $F_{10.7}$ = 120 sfu in Panels (d), (e), and (f), and $F_{10.7}$ = 200 sfu in Panels (g), (h), and (i) during quiet-time (t_1) in Panels (a), (d), and (g), storm-time (t_2) in Panels (b), (e), and (h), and recovery-time (t_3) in Panels (c), (f), and (i).

Fluence rates illustrated in Figures 11 and 12 are integrations in latitude and longitude at 1200 km of fluxes depicted in Figures 13 and 14 for summer and winter, respectively. Summer N^+ fluence rates are positive for all values of $F_{10.7}$ despite regions of negative (down-falling) flux seen particularly in the polar cap during recovery-time for $F_{10.7} = 200$ sfu, as seen in Panel (i) of Figure 13. Winter storm-time N^+ fluence rates are negative for $F_{10.7} = 120$ sfu where fluxes are negative in the regions of the cold N^+ TOI seen primarily in the noon polar cap sector of Panel (e) in Figure 14.

3.4 Data-Model Comparisons

This section validates the aforementioned simulations performed by HIDRA by comparing numerical results to reduced observations from Orbiting Geophysical Observatory 6 (OGO-6) and Atmosphere Explorer C (AE-C) satellites. Each observational data point from OGO-6 (launched in 1969) and AE-C (launched in 1973) is averaged over all geomagnetic activity, within 40 km altitude bins, and 6 hours local time centered at noon or midnight [M. Y. Lin et al., 2020]. During its first year of operation, the AE-C latitude of perigee was between 68° north and 60° south. The OGO-6 orbital inclination was 82° north which, by the dipole tilt, enabled OGO-6 to capture a large range of latitude [Taylor, 1971]. All densities of OGO-6 and AE-C were measured by a Bennet radio frequency ion mass spectrometer [Brinton et al., 1973] [Taylor, 1973] or a magnetic ion mass spectrometer [Hoffman et al., 1973]. In what follows, 7iPWOM noon solutions taken from [M. Y. Lin et al., 2020] are computed for stationary flux tubes at 80° north latitude at 12 hours MLT. Midnight solutions are averaged from two convecting flux tubes, one at 60-65° north latitude and another at 65-70° north latitude, near 0 hours MLT.

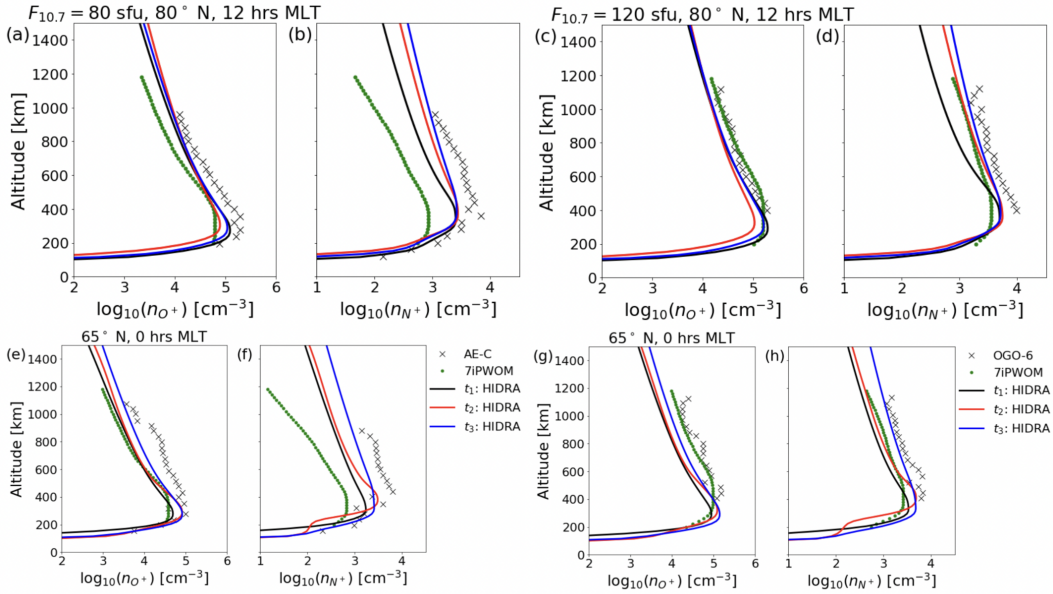

Figure 15: Data-model comparisons of HIDRA O^+ and N^+ density profiles during summer quiet-time (t_1), storm-time (t_2), and recovery-time (t_3), 7iPWOM, and AE-C or OGO-6 observations. $F_{10.7}$ = 80 sfu (AE-C) noon solutions are in Panels (a) and (b) and $F_{10.7}$ = 80 sfu (AE-C) midnight solutions are in Panels (e) and (f). $F_{10.7}$ = 120 sfu (OGO-6) noon solutions are in Panels (c) and (d) and $F_{10.7}$ = 120 sfu (OGO-6) midnight solutions are in Panels (g) and (h).

We present comparisons of O^+ and N^+ upflow solutions at noon and midnight sectors during northern hemisphere summer and winter from HIDRA versus 7iPWOM and observations from AE-C (for $F_{10.7}$ = 80 sfu) and from OGO-6 (for $F_{10.7}$ = 120 sfu). HIDRA noon O^+ and N^+ density profiles are for 80° north latitude and 12 hours MLT and midnight profiles are for 65° north latitude and 0 hours MLT. All simulations are parameterized as previously discussed. Since AE-C and OGO-6 observations are averaged over all geomagnetic conditions, we compare against HIDRA simulations for quiet-time (t_1), storm-time (t_2), and recovery-time (t_3) conditions seen in Figure 1.

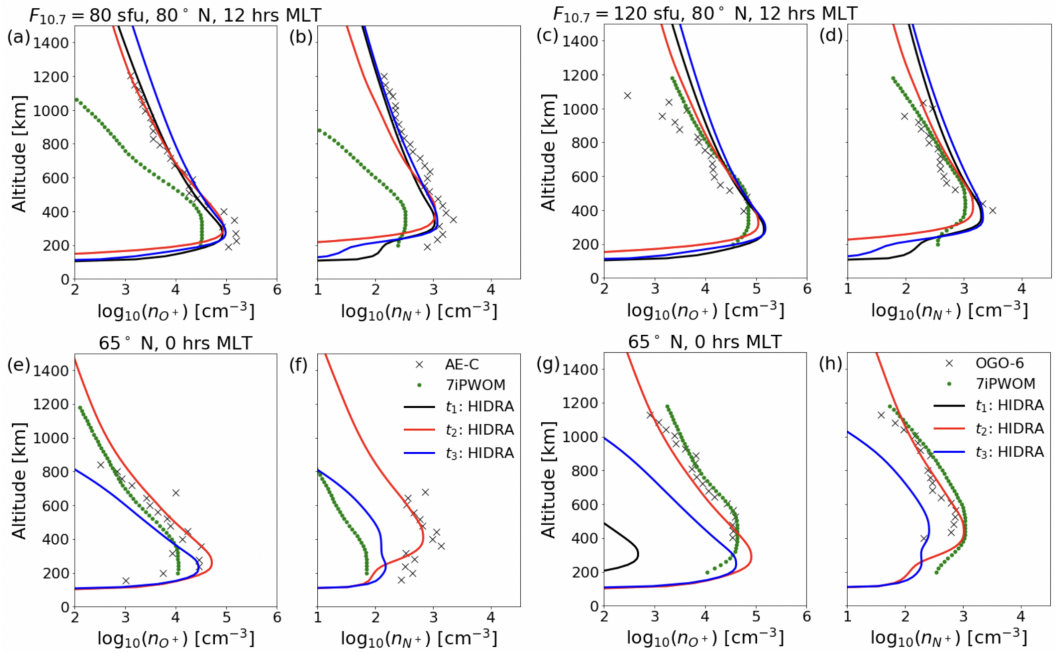

Figure 16: Data-model comparisons of HIDRA O^+ and N^+ density profiles during winter quiet-time (t_1), storm-time (t_2), and recovery-time (t_3), 7iPWOM, and AE-C or OGO-6 observations. $F_{10.7}$ = 80 sfu (AE-C) noon solutions are in Panels (a) and (b) and $F_{10.7}$ = 80 sfu (AE-C) midnight solutions are in Panels (e) and (f). $F_{10.7}$ = 120 sfu (OGO-6) noon solutions are in Panels (c) and (d) and $F_{10.7}$ = 120 sfu (OGO-6) midnight solutions are in Panels (g) and (h).

Figures 15 and 16 consistently show N^+ densities an order-of-magnitude less than O^+ densities for all conditions. HIDRA N^+ densities more closely represent observations than 7iPWOM, particularly for summer and winter noon and midnight cases of $F_{10.7}$ = 80 sfu and $F_{10.7}$ = 120 sfu, as seen in Panels (b) and (f) of Figures 15 and 16, respectively. In such cases, HIDRA N^+ densities are about an order-of-magnitude greater than for 7iPWOM, which results in a much closer approximation of observational data points. It is noted that summer recovery-time (t_3) N^+ densities most closely approximate observations, as seen in Panels (b), (d), (f), and (h) in Figure 15. Moreover, winter storm-time (t_2) N^+ densities most closely approximate observations, particularly for midnight solutions of Panels (f) and (h) in Figure 16. Strong convection is required to transport plasma to the winter midnight sector as suggested by the low O^+ and N^+ densities during winter quiet-time (t_1) for both $F_{10.7}$ = 80 sfu and $F_{10.7}$ = 120 sfu, as seen in Panels (e), (f), (g), and (h) in Figure 16. Although we do not validate HIDRA O^+ and N^+ temperatures versus observational temperature profiles, it is noted that HIDRA O^+ and N^+ scale heights more closely align with AE-C and OGO-6 than for 7iPWOM for all geomagnetic conditions, particularly for the winter noon case for $F_{10.7}$ = 80 sfu seen in Panels (a) and (b) of Figure 16.

4 Discussion

4.1 N^+ Production

This section investigates the significance of metastable chemical production of N^+ and its role in more closely matching observations. Although HIDRA and 7iPWOM differ in various way, a significant difference in the two models lies in the treatment of N^+ chemical production. Figure 17 shows sample N^+ chemical production and loss rate altitude profiles for summer storm-

time (t_2) at 80° north latitude and 12 hours MLT for $F_{10.7} = 120$ sfu in Panels (a) and (b), respectively. Of particular interest are the metastable N^+ chemical production terms:

$$O^+ + N(^2D) \rightarrow N^+ + O,$$
$$O^+(^2D) + N \rightarrow N^+ + O,$$
$$O_2^+ + N(^2D) \rightarrow N^+ + O_2.$$

The above reactions are not currently present in 7iPWOM. At local noon photoproduction of N^+ is significant, as expected, however, it is rivaled by O^++$N(^2D) \rightarrow N^+$+O chemical production at ~ 400 km. At ~ 800 km altitude, N^+ metastable chemical production by $O^+(^2D)$+$N \rightarrow N^+$+O is second to only photoproduction. O_2^++$N(^2D) \rightarrow N^+$+O_2 is a dominant metastable chemical production of N^+ below ~ 400 km.

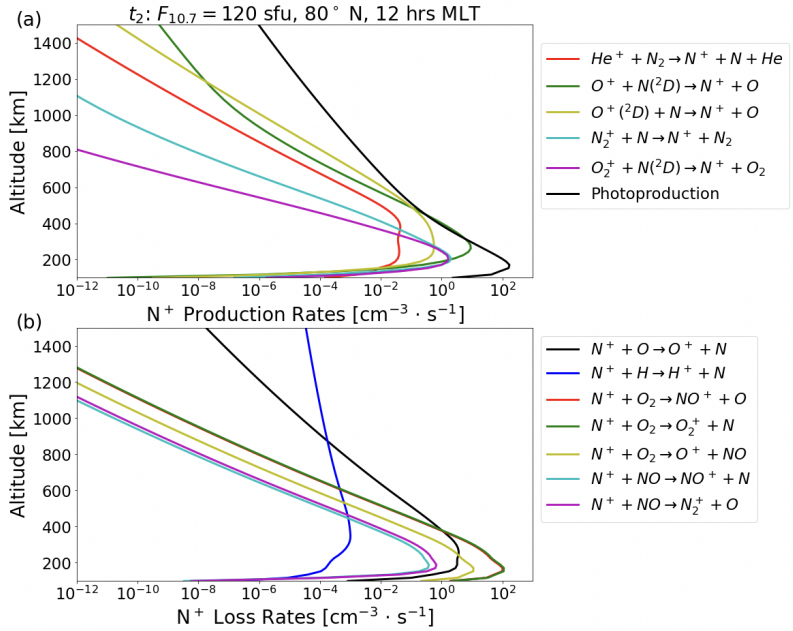

Figure 17: Altitude profiles of N^+ chemical production rates in Panel (a) and chemical loss rates in Panel (b) for summer noon storm-time (t_2) at 80° north latitude and for $F_{10.7} = 120$ sfu. Of particular interest are metastable chemical production rates of N^+: O^++$N(^2D) \rightarrow N^+$+O, $O^+(^2D)$+$N \rightarrow N^+$+O, and O_2^++$N(^2D) \rightarrow N^+$+O_2.

Figure 18 shows data-model comparisons of HIDRA O^+ and N^+ density profiles with metastable chemical production of N^+, HIDRA without the metastable chemical production of N^+ (labeled HIDRA†), and OGO-6 observations for summer, $F_{10.7} = 120$ sfu, noon at 80° north latitude in Panels (a) and (b), and midnight at 65° north latitude in Panels (c) and (d). The inclusion of metastable production of N^+ does not significantly alter the density profiles of O^+, however, they are critical in more closely representing observations for the density profiles of N^+. As seen in Panels (b) and (d), the scale heights are unaltered by the inclusion of metastable N^+ production, yet the densities of N^+ are increased by roughly half an order-of-magnitude when including the metastable production, as seen in the differences of HIDRA and HIDRA† for all geomagnetic conditions.

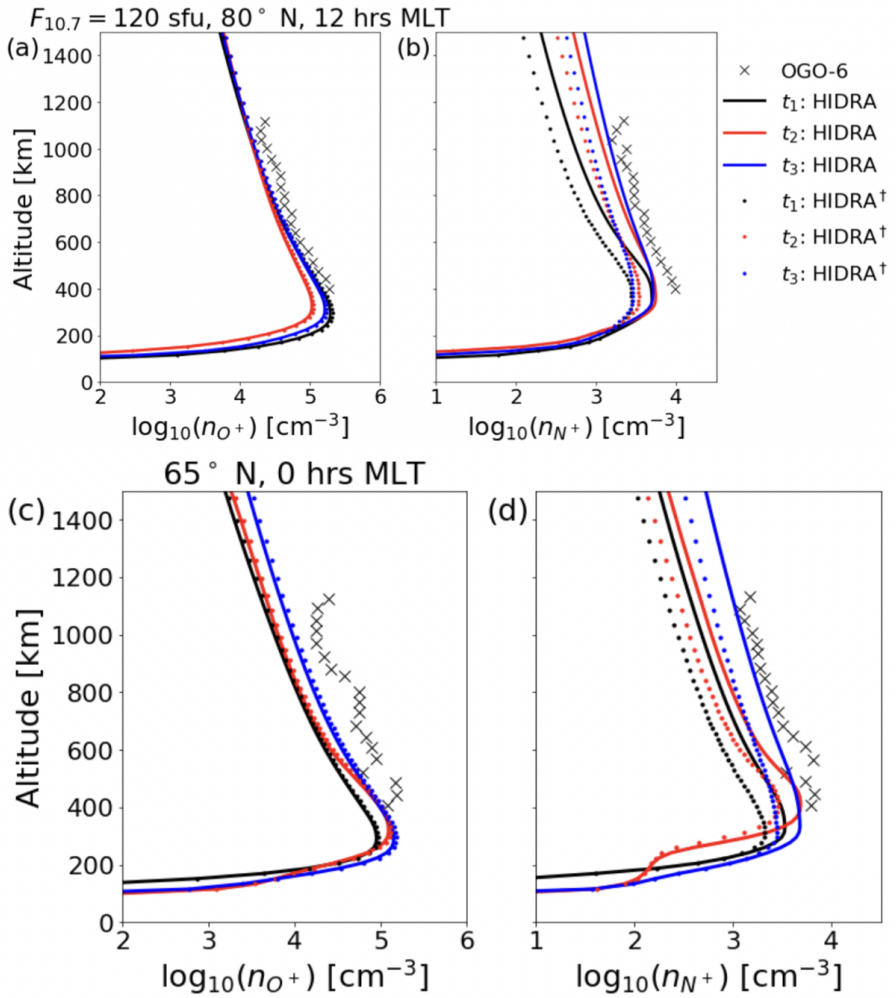

Figure 18: Data-model comparisons of HIDRA O^+ and N^+ density profiles with metastable N^+ production during summer quiet-time (t_1), storm-time (t_2), and recovery-time (t_3), and HIDRA† without metastable N^+ production, and OGO-6 observations. $F_{10.7}$ = 120 sfu noon solutions at 80° north latitude are in Panels (a) and (b) and $F_{10.7}$ = 120 sfu midnight solutions at 65° north latitude are in Panels (c) and (d).

4.2 N^+ Upflow Drivers

The relative roles of ion and electron pressure gradients in driving O^+ and N^+ upflows during quiet-time (t_1), storm-time (t_2), and recovery-time (t_3) geomagnetic conditions are investigated in this section. The sample case presented is for $F_{10.7}$ = 120 sfu at summer noon and 80° north latitude. Figures 19, 20, and 21 illustrate electron, H^+, He^+, O^+, and N^+ density and temperature profiles in Panels (a) and (b), respectively, and acceleration terms for O^+ and N^+ upflows in Panels (c) and (d) for quiet-time, storm-time, and recovery-time, respectively. In all presented cases, N^+ densities exceed He^+ densities. Above the collisional transition region, at ~ 1000 km, all collisional acceleration terms, a_{coll}, are negligible.

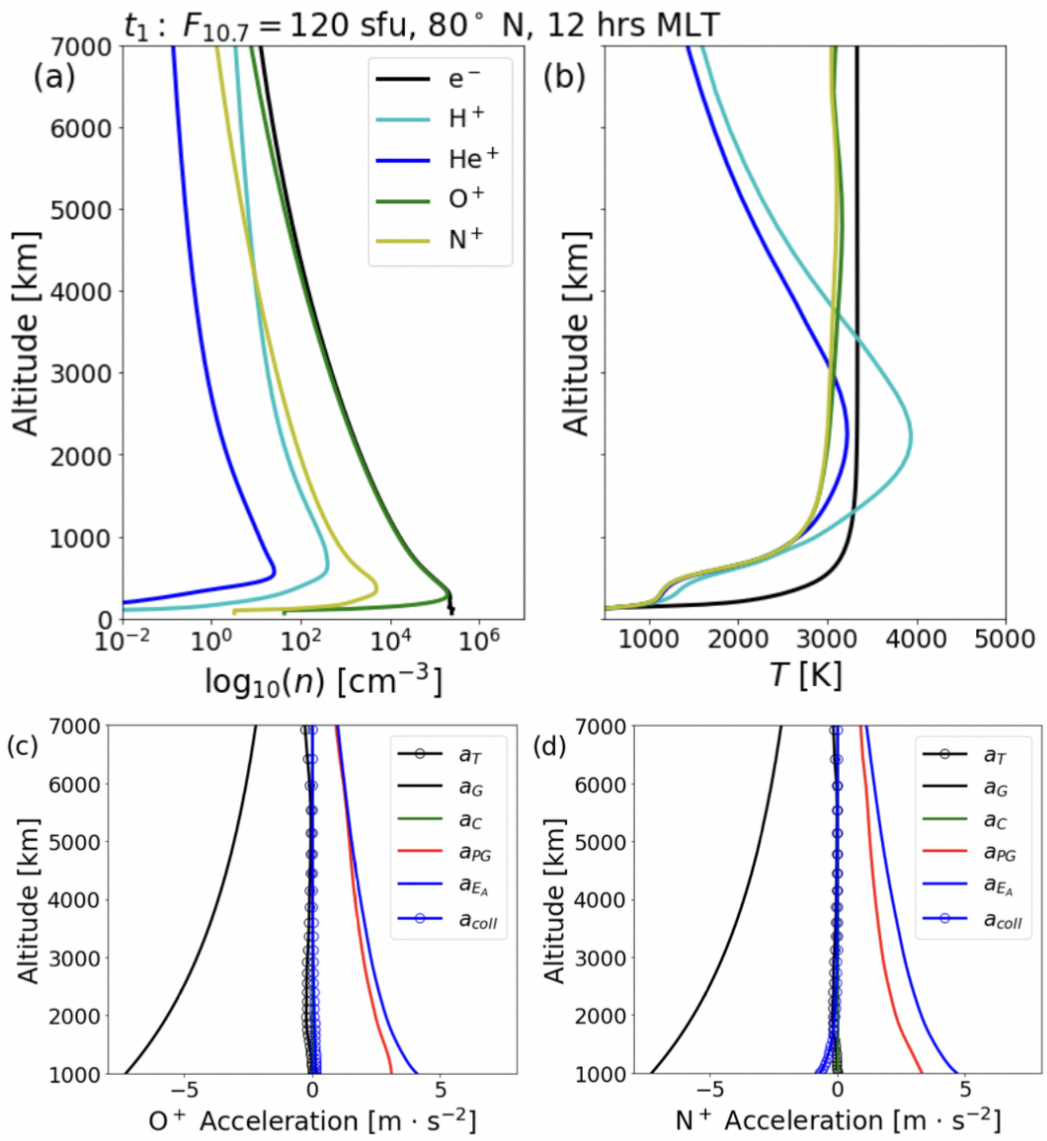

Figure 19: Summer quiet-time (t_1) conditions at 80° north latitude, 12 hours MLT, for $F_{10.7} = 120$ sfu. Density and temperature profiles of electrons, H^+, He^+, O^+, and N^+ are in Panels (a) and (b), respectively. O^+ and N^+ acceleration terms in Panels (c) and (d), respectively, where a_T is total acceleration, a_G is gravitational acceleration, a_C is centrifugal acceleration, a_{PG} is ion pressure gradient acceleration, a_{E_A} is electron pressure gradient acceleration, and a_{coll} is total collisional acceleration.

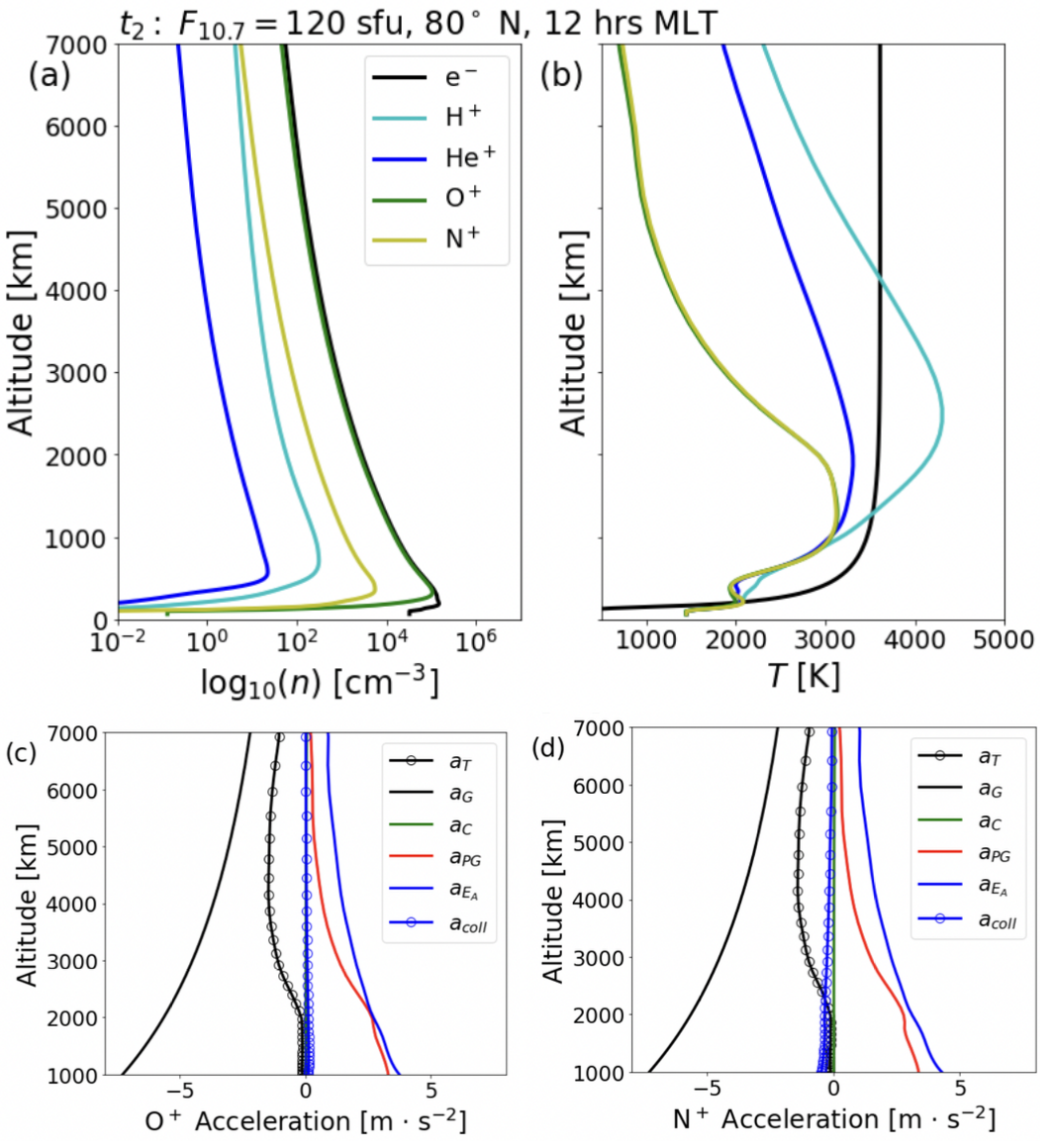

Figure 20: Summer storm-time (t_2) conditions at 80° north latitude, 12 hours MLT, for $F_{10.7}$ = 120 sfu. Density and temperature profiles of electrons, H^+, He^+, O^+, and N^+ are in Panels (a) and (b), respectively. O^+ and N^+ acceleration terms in Panels (c) and (d), respectively, where a_T is total acceleration, a_G is gravitational acceleration, a_C is centrifugal acceleration, a_{PG} is ion pressure gradient acceleration, a_{E_A} is electron pressure gradient acceleration, and a_{coll} is total collisional acceleration.

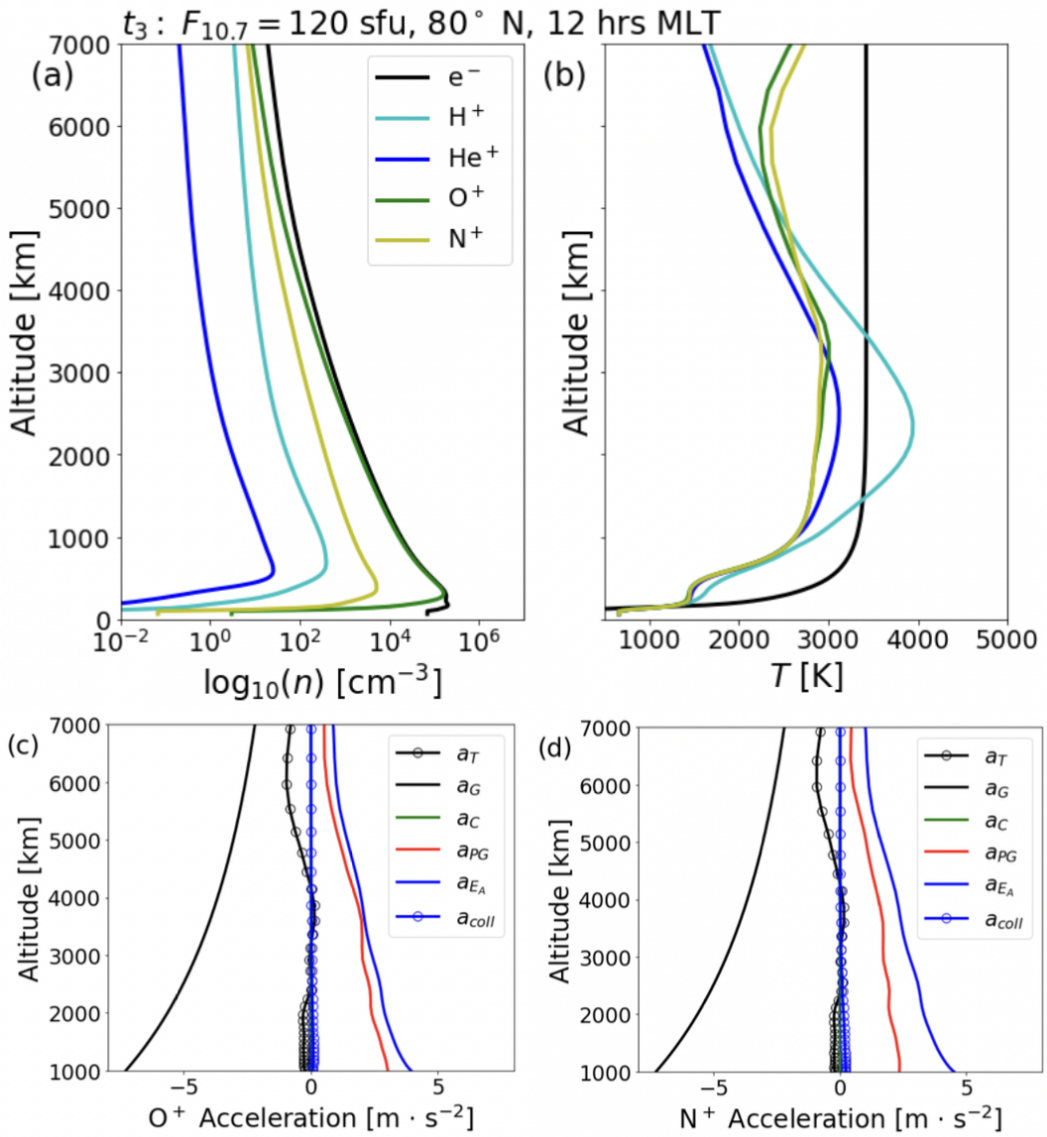

Figure 21: Summer recovery-time (t_3) conditions at 80° north latitude, 12 hours MLT, for $F_{10.7}$ = 120 sfu. Density and temperature profiles of electrons, H^+, He^+, O^+, and N^+ are in Panels (a) and (b), respectively. O^+ and N^+ acceleration terms in Panels (c) and (d), respectively, where a_T is total acceleration, a_G is gravitational acceleration, a_C is centrifugal acceleration, a_{PG} is ion pressure gradient acceleration, a_{E_A} is electron pressure gradient acceleration, and a_{coll} is total collisional acceleration.

Above ~ 1000 km the total acceleration, a_T, is dominated by a balance between gravitational acceleration, a_G, and combinations of ion pressure gradient accelerations, a_{PG} and electron pressure gradient (ambipolar electric field) accelerations, a_{E_A}. According to Panels (b) in Figures 19, 20, and 21, electron temperatures exceed both O^+ and N^+ temperatures. As a result, ambipolar electric field accelerations, a_{E_A}, exceed ion pressure gradient accelerations, a_{PG}, both O^+ and N^+ upflows, as seen in Panels (c) and (d) of Figures 19, 20, and 21. Panels (c) and (d) of Figure 19 show that quiet-time total O^+ and N^+ accelerations, a_T, are approximately zero denoting flux-tubes in near-equilibrium. During storm-time, a_T is dominated by gravity such that the flux-tubes are not in equilibrium above ~ 2000 km, as seen in Panels (c) and (d) of Figure

20. A similar case represents the transient equilibrium of O^+ and N^+ above $\sim$ 4000 km for recovery-time, as seen in Panels (c) and (d) of Figure 21. At all three geomagnetic conditions, the O^+ and N^+ temperatures are near identical and electron temperatures exceed both O^+ and N^+ temperatures. For such conditions, both O^+ and N^+ upflows are Type II, that is, driven by field-aligned ambipolar electric fields caused by electron precipitation.

5 Conclusions

In this study, HIDRA, part of the MAGE framework from the Center for Geospace Storms (CGS) NASA DRIVE Science Center, is employed to investigate the production mechanisms and upflow drivers of N^+ upflows of the terrestrial polar wind for summer and winter conditions in the northern hemisphere under various solar activity levels and geomagnetic conditions. Relative abundances of N^+ are scrutinized in the dominance of O^+. It is numerically demonstrated that relative N^+ to O^+ densities are greatest for $F_{10.7} = 80$ sfu at recovery-time, where n_{N^+}/n_{O^+} values are $\sim$ 15-30%. Although O^+ and N^+ densities increase with solar activity, relative concentrations n_{N^+}/n_{O^+} are greater for lower $F_{10.7}$ during summer and winter over all geomagnetic conditions. During summer, N^+ densities at quiet-time are $\sim$ 50-100% N^+ densities at storm-time and quiet-time N^+ concentrations during winter may exceed those at storm-time by up to $\sim$ 300%. N^+ density ratios at quiet-time to storm-time remain largely unaltered with solar activity for both summer and winter. This is in agreement with findings by [Hoffman, 1970] [Hoffman et al., 1974].

N^+ densities are consistently $\sim$ 10% of O^+ densities for $F_{10.7} = 80$ sfu, $F_{10.7} = 120$ sfu, and $F_{10.7} = 200$ sfu. This is in agreement with numerical studies by [M. Y. Lin et al., 2020] and early measurements by OGO-2 [Brinton et al., 1968], Explorer 31 [Hoffman, 1967] [Hoffman, 1970], and ISIS-2 [Hoffman et al., 1974]. Furthermore, fluence rates of N^+ qualitatively resemble those of O^+ at $\sim$ 10% the total fluence rate. This demonstrates the behavior of N^+ as a 'light version' of O^+ rather than a 'heavy version' of He^+. Although 7iPWOM and HIDRA treat N^+ chemical production differently, current 7iPWOM does not include metastable N^+ production and thus 7iPWOM N^+ densities are signficantly less than observations by OGO-6 and AE-C. The inclusion of metastable chemical production of N^+ is critical to more closely reproduce observations, primarily the inclusion of the following reactions: $O^+ + N(^2D) \rightarrow N^+ + O$, $O^+(^2D) + N \rightarrow N^+ + O$, and $O_2^+ + N(^2D) \rightarrow N^+ + O_2$. Finally, as for O^+, N^+ upflows are driven primarily by a combination of electron and ion pressure gradients above the collisional transition region. Under most conditions, N^+ densities exceed He^+ densities, in agreement with 7iPWOM simulations [M. Y. Lin et al., 2020].

6 Acknowledgements

This work is supported by the NASA DRIVE Science Center for Geospace Storms (CGS) under award 80NSSC22M0163. RHV is additionally supported by the National Science Foundation Faculty Development in Space Sciences award AGS-1936186. Special Acknowledgements go to Viacheslav Merkin, Micheal Wiltberger, Kareem Sorathia, and the entire CGS team.

Open Research

References

André, M., Norqvist, P., Andersson, L., Eliasson, L., Eriksson, A. I., Blomberg, L., … Waldemark, J. (1998). Ion energization mechanisms at 1700 km in the auroral region. *Journal of Geophysical Research*, *103*(4199-4222).

André, M., & Yau, A. W. (1997). Theories and observations of ion energization and outflows in the high latitude magnetosphere. *Space Science Reviews*, *80*, 27-48.

Bao, S. (2019). *Large-scale coupled models of the inner magnetosphere.* (Unpublished doctoral dissertation). Rice University.

Bashir, M. F., & Ilie, R. (2018). A new N+ band of electromagnetic ion cyclotron waves in multi-ion cold plasmas. *Geophysical Research Letters*, *45*, 10150-10159.

Bouhram, M., Malingre, M., Jasperse, J. R., & Dubouloz, N. (2003). Modeling transverse heating and outflow of ionospheric ions from the dayside cusp/cleft. 1 A parametric study. *Annales Geophysicae*, *21*, 1753-1771.

Brinton, H. C., Grebowsky, J. M., & Mayr, H. G. (1971). Altitude variation of ion composition in the midlatitude trough region: Evidence for upward plasma flow. *Journal of Geophysical Research*, *76*, 3738-3745.

Brinton, H. C., Pharo, M. W. I., Rahman, N. K., & Taylor, H. A. J. (1968). *Latitudinal variation of the composition of the topside ionosphere, first results of the OGO-2 ion spectrometer.* Retrieved from `https://ntrs.nasa.gov/citations/19680016284`

Brinton, H. C., Scott, L. R., Pharo, M. W., & Coulson, J. T. (1973). The Bennet ion-mass spectrometer on Atmosphere Explorer-C and E. *Radio Science*, *8*(4), 323-332.

Burns, A. G., Solomon, S. C., Wang, W., Qian, L., Zhang, Y., Paxton, L. J., … Liu, H. L. (2015). Explaining solar cycle effects on composition as it relates to the winter anomaly. *Journal of Geophysical Research- Space Physics*, *120*(7), 5253-6044.

Chappell, C. R., Moore, T. E., & Waite, J. H. (1987). The ionosphere as a fully adequate source of plasma for the Earth's magnetosphere. *Journal of Geophysical Research*, *92*, 5896-5910.

Collin, H. L., Peterson, W. K., Lennartsson, O. W., & Drake, J. F. (1998). The seasonal variation of auroral ion beams. *Geophysical Research Letters*, *25*, 4071.

Crew, G. B., Chang, T., & Retterer, J. M. (1990). Ion cyclotron resonance heated conics: Theory and observations. *Journal of Geophysical Research*, *95*(A4), 3959-3985.

Daglis, I. A., Thorne, R. M., Baumjohann, W., & Orsini, S. (1999). The terrestrial ring current: Origin, formation, and decay. *Reviews of Geophysics*, *37*, 407-438.

Dessler, A. J., & Michel, F. C. (1966). Plasma in the geomagnetic tail. *Journal of Geophysical Research*, *71*(1421).

Eastman, T. E., Frank, L. A., & Huang, C. Y. (1985). The boundary layers as the primary transport regions of the Earth's magnetotail. *Journal of Geophysical Research*, *90*, 9541.

Fang, X., Randall, C. E., Lummerzheim, D., Solomon, S. C., Mills, M. J., Marsh, D. R., … Lu, G. (2008). Electron impact ionization: A news parameterization for 100 eV to 1 MeV electrons. *Journal of Geophysical Research*, *113*(A09311).

Foster, C., & Lester, M. (1996). Observations of nightside auroral plasma upflows in the F-region and topside ionosphere. *Annals of Geophysics*, *14*, 1274-1283.

Garcia, K. S., Merkin, V. G., & Hughes, W. J. (2010). Effects of nightside O+ outflow on magnetospheric dynamics: Results of multifluid MHD modeling. *Journal of Geophysical Research*, *115*(A00J09).

Glocer, A., Toth, G., Ma, Y., Gombosi, T., Zhang, J. C., & Kistler, L. M. (2009). Multifluid block-adaptive-tree solar wind roe-type upwind scheme: Magnetospheric composition and dynamics during geomagnetic storms-Initial results. *Journal of Geophysical Research*, *114*(A12203).

Hamilton, D. C., Gloeckler, G., Ipavich, F. M., Wilken, B., & Stuedemann, W. (1988). Ring current development during the great geomagnetic storm of February 1986. *Journal of Geophysical Research*, *93*, 14343-14355.

Hoffman, J. H. (1967). Composition measurements of the topside ionosphere. *Science*, *155*(3760), 322-324.

Hoffman, J. H. (1970). Studies of the composition of the ionosphere with a magnetic deflection mass spectrometer. *International Journal of Mass Spectrometery and Ion Physics*, *4*, 315-322.

Hoffman, J. H., Dodson, W. H., Lippincott, C. R., & Hammack, H. D. (1974). Initial ion composition results from the ISIS 2 satellite. *Journal of Geophysical Research*, *79*, 4246-4251.

Hoffman, J. H., Hanson, W. B., Lippincott, C. R., & Ferguson, E. E. (1973). The magnetic ion-mass spectrometer on Atmosphere Explorer. *Radio Science*, *8*(4), 315-322.

Huddleston, M. M., Chappell, C. R., Delcourt, D. C., Moore, T. E., Giles, B. L., & Chandler, M. O. (2005). An examination of the process and magnitude of ionospheric plasma supply to the magnetosphere. *Journal of Geophysical Research*, *110*(A12202).

Ilie, R., & Liemohn, M. W. (2016). The outflow of ionospheric nitrogen ions: A possible tracer for the altitude-dependent transport and energization processes of ionospheric plasma. *Journal of Geophysical Research- Space Physics*, *121*, 9250-9255.

Ilie, R., Skoug, R. M., Funsten, H. O., Liemohn, M. W., Bailey, J. J., & Gruntman, M. (2013). The impact of geocoronal density on ring current development. *Journal of Atmospheric and Solar-Terrestrial Physics*, *99*, 92-103.

Keika, K., Brandt, P. C., Nosé, M., & Mitchell, D. G. (2011). Evolution of ring current ion energy spectra during the storm recovery phase: Implication for dominant ion loss processes. *Journal of Geophysical Research- Space Physics*, *116*.

Kintner, P. M., Bonnell, J., Arnoldy, R., Lynch, K., Pollock, C., & Moore, T. (1996). SCIFER- transverse ion acceleration and plasma waves. *Geophysical Research Letters*, *23*, 1873-1876.

Kistler, L. M., Ipavich, F. M., Hamilton, D. C., Gloeckler, G., Wilken, B., Kremser, G., & Stuedemann, W. (1989). Energy spectra of the major ion species in the ring current during geomagnetic storms. *Journal of Geophysical Research*, *94*(A4), 3579.

Kivelson, M. G., & Spence, H. E. (1988). On the possibility of quasi-static convection in the quiet magnetotail. *Geophysical Research Letters*, *15*, 1541.

Lennartsson, O. W. (2001). Ion composition aspects of magnetotail plasma flows. *Journal of Geophysical Research*, *106*(15), 621.

Liemohn, M. W., Kozyra, J. U., Jordanova, V. K., Khazanov, G. V., Thomsen, M. F., & Cayton, T. E. (1999). Analysis of early phase ring current recovery mechanisms during geomagnetic storms. *Geophysical Research Letters*, *26*, 2845-2848.

Lin, D., Sorathia, K., Wang, W., Merkin, V., Bao, S., Pham, K., … Anderson, B. (2021). The Role of Diffuse Electron Precipitation in the Formation of Subauroral Polarization Streams. *Journal of Geophysical Research- Space Physics*, *126*(11).

Lin, D., Wang, W., Garcia-Sage, K., Yue, J., Merkin, V., McInerney, J. M., … Sorathia, K. (2022). Thermospheric Neutral Density Variation During the "SpaceX" Storm: Implications From Physics-Based Whole Geospace Modeling. *Space Weather*, *20*(12).

Lin, M. Y., Ilie, R., & Glocer, A. (2020). The contribution of N+ ions to Earth's polar wind. *Geophysical Research Letters*, *47*.

Liu, X., Wang, W., Thayer, J. P., Burns, A., Sutton, E., Solomon, S. C., … Lucas, G. (2014). The winter helium bulge revisited. *Geophysical Research Letters*, *41*(19), 6603-6609.

Lockwood, M., Waite, J. H., Moore, T. E., Johnson, J. F. E., & Chappell, C. R. (1985). A new source of suprathermal O^+ ions near the dayside polar cap boundary. *Journal of Geophysical Research*, *90*, 4099.

Lynch, K. A., Arnoldy, R. L., Kintner, P. M., & Bonnell, J. (1996). The AMICIST auroral sounding rocket: a comparison of transverse ion acceleration mechanisms. *Geophysical Research Letters*, *23*, 3293-3296.

Lynch, K. A., Arnoldy, R. L., Kintner, P. M., Schuck, P., Bonnell, J. W., & Coffey, V. (1999). Auroral ion acceleration from lower hybrid solitary structure: a summary of sounding rocket observations. *Journal of Geophysical Research*, *104*(A12), 28151-28534.

McFadden, J. P., Carlson, C. W., Ergun, R. E., Mozer, F. S., Temerin, M., Peria, W., … Pfaff, R. (1998). Spatial structure and gradients of ion beams observed by FAST. *Geophysical Research Letters*, *25*(12), 2012-2024.

Merkin, V. G., & Lyon, J. G. (2010). Effects of the low-latitude ionospheric boundary condition on the global magnetosphere. *Journal of Geophysical Research- Space Physics*, *115*(A10).

Nishida, A. (1966). Formation of a plasmapause or magnetospheric plasma knee by combined action of magnetospheric convection and plasma escape from the tail. *Journal of Geophysical Research*, *71*(5669).

Nosé, M., Taguchi, S., Hosokawa, K., Christon, S. P., McEntire, R. W., Moore, T. E., & Col-

lier, M. R. (2005). Overwhelming O+ contribution to the plasma sheet energy density during the October 2003 superstorm: Geotail/EPIC and IMAGE/LENA observations. *Journal of Geophysical Research*, *110*(A09S24).

Nossal, S. M., Mierkiewicz, E. J., & Roesler, F. L. (2012). Observed and modeled solar cycle variation in geocoronal hydrogen using NRLMSISE-00 thermosphere conditions and the Bishop analytic exosphere model. *Journal of Geophysical Research- Space Physics*, *117*(A3).

Ogawa, Y., Fujii, R., Buchert, S. C., Nozawa, S., & Ohtani, S. (2003). Simultaneous EISCAT Svalbard radar and DMSP observations of ion upflow in the dayside polar ionosphere. *Journal of Geophysical Research- Space Physics*, *108*, 1101.

Pham, K. H., Zhang, B., Sorathia, K., Dang, T., Wang, W., Merkin, V., … Lyon, J. (2022). Thermospheric Density Perturbations Produced by Traveling Atmospheric Disturbances During August 2005 Storm. *Journal of Geophysical Research- Space Physics*, *127*(2).

Picone, J. M., Hedin, A. E., Drob, D. P., & Aikin, A. C. (2002). Nrlmsise-00 empirical model of the atmosphere: Statistical comparisons and scientific issues. *Journal of Geophysical Research*, *107*(1468).

Pokhotelov, D., Fernandez-Gomez, I., & Borries, C. (2021). Polar tongue of ionisation during geomagnetic superstorm. *Annales Geophysicae*, *39*, 833-847.

Richards, P. G. (2011). Reexamination of ionospheric photochemistry. *Journal of Geophysical Research*, *116*(A08307).

Richards, P. G., Woods, T. N., & Peterson, W. K. (2006). Heuvac: A new high resolution solar euv proxy model. *Advances in Space Research*, *37*, 315-322.

Sharp, R. D., Johnson, R. G., & Shelley, E. G. (1977). Observations of an ionospheric acceleration mechanism producing energetic (keV) ions primarily normal to the geomagnetic field direction. *Journal of Geophysical Research*, *82*, 3324.

Shelley, E. G., Johnson, R. G., & Sharp, R. D. (1972). Satellite observations of energetic heavy ions during a geomagnetic storm. *Journal of Geophysical Research*, *77*, 6104.

Shelley, E. G., Sharp, R. D., & Johnson, R. G. (1976). Satellite observations of an ionospheric acceleration mechanism. *Geophysical Research Letters*, *3*, 654.

Strangeway, R. J., Ergun, R. E., Su, Y. J., Carlson, C. W., & Elphic, R. C. (2005). Factors controlling ionospheric outflows as observed at intermediate altitudes. *Journal of Geophysical Research*, *110*.

Su, Y. J., Canton, R. G., Horwitz, J. L., & Richards, P. G. (1999). Systematic modeling of soft-electron precipitation effects on high-latitude F region and topside ionospheric upflows. *Journal of Geophysical Research*, *104*, 153-163.

Summers, D., Ni, B., & Meredith, N. P. (2007). Timescales for radiation belt electron acceleration and loss due to resonant wave-particle interactions: 2. Evaluation for VLF chorus, elf hiss, and electromagnetic ion cyclotron waves. *Journal of Geophysical Research*, *112*(A04207).

Taylor, H. A. (1971). Observed solar geomagnetic control of the ionosphere- implications for reference ionospheres. *Advances in Space Research*, *12*, 1275-1290.

Taylor, H. A. (1973). Parametric description of thermospheric ion composition results. *Journal of Geophysical Research*, *78*(1), 315-319.

Thelin, B., Aparicio, B., & Lundin, R. (1990). Observations of upflowing ionospheric ions in the mid-altitude cusp/cleft region with the Viking satellite. *Journal of Geophysical Research*, *95*, 5931-5939.

Toffoletto, F., Sazykin, S., & Spiro, R. (2003). Inner magnetospheric modeling with the Rice Convection Model. *Space Science Reviews*, *107*, 175-196.

Varney, R. H., Solomon, S. C., & Nicolls, M. J. (2014). Heating of the sunlit polar cap ionosphere by reflected photoelectrons. *Journal of Geophysical Research- Space Physics*, *119*, 8660-8684.

Varney, R. H., Wiltberger, M., & Lotko, W. (2015). Modeling the interaction between convection and nonthermal ion outflows. *Journal of Geophysical Research- Space Physics*, *120*, 2353-2362.

Varney, R. H., Wiltberger, M., Zhang, B., Lotko, W., & Lyon, J. (2016). Influence of ion outflow in coupled geospace simulations: 1. Physics-based ion outflow model development and sensitivity study. *Journal of Geophysical Research- Space Physics*, *121*, 9671-9687.

Wahlund, J. E., Opgenoorth, H. J., Haggstrom, I., Winser, K. J., & Jones, G. O. L. (1992). EISCAT observations of topside ionospheric ion outflows during auroral activity: revisited. *Journal of Geophysical Research*, *97*, 3019-3037.

Wiltberger, M., Lotko, W., Lyon, J. G., Damiano, P., & Merkin, V. (2010). Influence of cusp O+ outflow on magnetotail dynamics in a multifluid MHD model of the magnetosphere. *Journal of Geophysical Research*, *115*(A00J05).

Winglee, R. M., Chua, D., Brittnacher, M., Parks, G. K., & Lu, G. (2002). Global impact of ionospheric outflows on the dynamics of the magnetosphere and cross-polar cap potential. *Journal of Geophysical Research*, *107*(1237).

Yamauchi, M. (2019). Terrestrial ion escape and relevant circulation in space. *Annales Geophysicae*, *37*(6), 1197-1222.

Yau, A. W., & Andre, M. (1997). Sources of ion outflow in the high latitude ionosphere. *Space Science Reviews*, *80*(1).

Yau, A. W., Peterson, W. K., & Shelley, E. G. (1988). Quantitative parameterization of energetic ionospheric ion outflow. *Geophysical Monograph*(44).

Yau, A. W., Shelley, E. G., Peterson, W. K., & Lenchyshyn, L. (1985). Energetic auroral and polar ion outflow at DE-1 altitudes: Magnitude, composition, magnetic activity dependence and long-term variations. *Journal of Geophysical Research*, *90*, 8417.

Zettergren, M., & Semeter, J. (2012). Ionospheric plasma transport and loss in auroral downward current regions. *Journal of Geophysical Research- Space Physics*, *117*(A6), 6306.

Zhang, B., Lotko, W., Brambles, O., Wiltberger, M., & Lyon, J. (2015). Electron precipitation models in global magnetosphere simulations. *Journal of Geophysical Research-Space Physics*, *120*, 1035-1056.

Zhang, B., Sorathia, K. A., Lyon, J. G., Merkin, V. G., Garretson, J. S., & Wiltberger, M. (2019). GAMERA: A Three-dimensional Finite-volume MHD Solver for Non-orthogonal Curvilinear Geometries. *The Astrophysical Journal Supplement Series*, *224*(20).

Zheng, Y., Moore, T. E., Mozer, F. S., Russell, C. T., & Strangeway, R. J. (2005). Polar study of ionospheric ion outflow versus energy input. *Journal of Geophysical Research*, *110*.